

ALICE-ANA-2016-xxx
June 1, 2017

Lambda-Kaon and Cascade-Kaon Femtoscopy in Pb-Pb Collisions at $\sqrt{s_{NN}} = 2.76$ TeV from the LHC ALICE Experiment

Jesse T. Buxton¹

1. Department of Physics, The Ohio State University, Columbus, Ohio, USA

Email: jesse.thomas.buxton@cern.ch

Abstract

We present results from a femtoscopic analysis of Lambda-Kaon correlations in Pb-Pb collisions at $\sqrt{s_{NN}} = 2.76$ TeV by the ALICE experiment at the LHC. All pair combinations of Λ and $\bar{\Lambda}$ with K^+ , K^- and K_S^0 are analyzed. The femtoscopic correlations are the result of strong final-state interactions, and are fit with a parametrization based on a model by R. Lednicky and V. L. Lyuboshitz [1]. This allows us to both characterize the emission source and measure the scattering parameters for the particle pairs. We observe a large difference in the Λ - K^+ ($\bar{\Lambda}$ - K^-) and Λ - K^- ($\bar{\Lambda}$ - K^+) correlations in pairs with low relative momenta ($k^* \lesssim 100$ MeV). Additionally, the average of the Λ - K^+ ($\bar{\Lambda}$ - K^-) and Λ - K^- ($\bar{\Lambda}$ - K^+) correlation functions is consistent with our Λ - K_S^0 ($\bar{\Lambda}$ - K_S^0) measurement. The results suggest an effect arising from different quark-antiquark interactions in the pairs, i.e. $s\bar{s}$ in Λ - K^+ ($\bar{\Lambda}$ - K^-) and $u\bar{u}$ in Λ - K^- ($\bar{\Lambda}$ - K^+). To gain further insight into this hypothesis, we currently are conducting a Ξ -K femtoscopic analysis.

Contents

1	Introduction	4
2	Data Sample and Software	4
2.1	Data Sample	4
2.2	Software	4
3	Data Selection	5
3.1	Event Selection and Mixing	5
3.2	K $^{\pm}$ Track Selection	5
3.3	V0 Selection	7
3.3.1	Λ Reconstruction	7
3.3.2	K $_S^0$ Reconstruction	9
3.4	Cascade Reconstruction	12
3.5	Pair Selection	14
4	Correlation Functions	15
5	Fitting	16
5.1	Model: ΛK $_S^0$, ΛK $^{\pm}$, Ξ ch K $_S^0$	16
5.2	Model: Ξ ch K ch	19
5.3	Momentum Resolution Corrections	22
5.4	Residual Correlations	23
6	Systematic Errors	26
6.1	Systematic Errors: ΛK $_S^0$	27
6.1.1	Particle and Pair Cuts	27
6.1.2	Non-Flat Background	28
6.1.3	Fit Range	28
6.2	Systematic Errors: ΛK $^{\pm}$	28
6.2.1	Particle and Pair Cuts	28
6.2.2	Non-Flat Background	28
6.2.3	Fit Range	28
6.3	Systematic Errors: ΞK $^{\pm}$	28
6.3.1	Particle and Pair Cuts	28

6.3.2	Non-Flat Background	29
6.3.3	Fit Range	29
7	Results and Discussion	29
7.1	Results: ΛK_S^0 and ΛK^\pm	29
7.2	Results: ΞK^\pm	38
8	To Do	38

List of Figures

1	V0 Reconstruction	7
2	K_S^0 contamination in $\Lambda(\bar{\Lambda})$ collection	9
3	Λ and $\bar{\Lambda}$ Purity	9
4	$\Lambda(\bar{\Lambda})$ contamination in K_S^0 collection	11
5	K_S^0 Purity	12
6	Ξ Reconstruction	13
7	$\Xi^-(\bar{\Xi}^+)$ Purity	14
8	Average Separation of $\Lambda(\bar{\Lambda})$ and K_S^0 Daughters	15
9	Average Separation of $\Lambda(\bar{\Lambda})$ Daughter and K^\pm	16
10	Average Separation of Ξ Daughters and K^\pm	17
11	$\Lambda(\bar{\Lambda})K_S^0$ Correlation Functions	18
12	ΛK^+ and $\bar{\Lambda} K^-$ Correlation Functions	19
13	ΛK^- and $\bar{\Lambda} K^+$ Correlation Functions	20
14	Correlation Functions: ΛK^+ vs ΛK^- for 0-10% Centrality	21
15	Momentum Resolution: Sample k_{True}^* vs. k_{Rec}^*	24
16	Particle Contaminations Visible in k_{True}^* vs. k_{Rec}^*	25
17	Transform Matrices for ΛK^+ Analysis	26
18	Transform Matrices for $\bar{\Lambda} K^+$ Analysis	27
19	$\Lambda K_S^0(\bar{\Lambda} K_S^0)$ Fits	30
20	$\Lambda K_S^0(\bar{\Lambda} K_S^0)$ Fits (Wide Range)	31
21	$\Lambda K^+(\bar{\Lambda} K^-)$ Fits	32
22	$\Lambda K^+(\bar{\Lambda} K^-)$ Fits (Wide Range)	33
23	$\Lambda K^-(\bar{\Lambda} K^+)$ Fits	34
24	$\Lambda K^-(\bar{\Lambda} K^+)$ Fits (Wide Range)	35
25	ΞK^\pm Results	38
26	ΞK^\pm Coulomb Only	39
27	ΞK^\pm Coulomb Only	40

12 1 Introduction

13 NOTE: An updated version of this analysis note should be uploaded before 16 December 2016. Amongst
 14 other additions, this new version will include more thorough results and discussion of our ΞK^\pm analyses.
 15 If possible, we would like to at least show the data from this study, and possibly even preliminary results.
 16 However, with QM deadlines close approaching, this may not be possible.

17 We present results from a femtoscopic analysis of Lambda-Kaon correlations in Pb-Pb collisions at $\sqrt{s_{NN}}$
 18 = 2.76 TeV by the ALICE experiment at the LHC. All pair combinations of Λ and $\bar{\Lambda}$ with K^+ , K^- and
 19 K_S^0 are analyzed. The femtoscopic correlations are the result of strong final-state interactions, and are
 20 fit with a parametrization based on a model by R. Lednický and V. L. Lyuboshitz [1]. This allows us to
 21 both characterize the emission source and measure the scattering parameters for the particle pairs. We
 22 observe a large difference in the Λ - K^+ ($\bar{\Lambda}$ - K^-) and Λ - K^- ($\bar{\Lambda}$ - K^+) correlations in pairs with low relative
 23 momenta ($k^* \lesssim 100$ MeV). Additionally, the average of the Λ - K^+ ($\bar{\Lambda}$ - K^-) and Λ - K^- ($\bar{\Lambda}$ - K^+) correlation
 24 functions is consistent with our Λ - K_S^0 ($\bar{\Lambda}$ - K_S^0) measurement. The results suggest an effect arising from
 25 different quark-antiquark interactions in the pairs, i.e. $s\bar{s}$ in Λ - K^+ ($\bar{\Lambda}$ - K^-) and $u\bar{u}$ in Λ - K^- ($\bar{\Lambda}$ - K^+). To
 26 gain further insight into this hypothesis, we currently are conducting a Ξ - K femtoscopic analysis.

27 2 Data Sample and Software

28 2.1 Data Sample

29 The analysis used “pass 2” reconstructed Pb-Pb data from LHC11h (AOD145). The runlist was selected
 30 from runs with global quality tag “1” in the ALICE Run Condition Table. Approximately 40 million
 31 combined central, semi-central, and minimum bias events were analyzed. Runs from both positive (++)
 32 and negative (--) magnetic field polarity settings were used.

33 Run list: 170593, 170572, 170388, 170387, 170315, 170313, 170312, 170311, 170309, 170308, 170306,
 34 170270, 170269, 170268, 170230, 170228, 170207, 170204, 170203, 170193, 170163, 170159, 170155,
 35 170091, 170089, 170088, 170085, 170084, 170083, 170081, 170040, 170027, 169965, 169923, 169859,
 36 169858, 169855, 169846, 169838, 169837, 169835, 169591, 169590, 169588, 169587, 169586, 169557,
 37 169555, 169554, 169553, 169550, 169515, 169512, 169506, 169504, 169498, 169475, 169420, 169419,
 38 169418, 169417, 169415, 169411, 169238, 169167, 169160, 169156, 169148, 169145, 169144, 169138,
 39 169099, 169094, 169091, 169045, 169044, 169040, 169035, 168992, 168988, 168826, 168777, 168514,
 40 168512, 168511, 168467, 168464, 168460, 168458, 168362, 168361, 168342, 168341, 168325, 168322,
 41 168311, 168310, 168115, 168108, 168107, 168105, 168076, 168069, 167988, 167987, 167985, 167920,
 42 167915

43 Analysis was also performed on the LHC12a17a_fix (AOD149) Monte Carlo HIJING events for certain
 44 checks. THERMINATOR2 was also used for certain aspects, such as transform matrices described feed-
 45 down contributions.

46 2.2 Software

47 The analysis was performed on the PWGCF analysis train using AliRoot v5-08-18-1 and AliPhysics
 48 vAN-20161027-1.

49 The main classes utilized include: AliFemtoVertexMultAnalysis, AliFemtoEventCutEstimators, AliFem-
 50 toESDTrackCutNSigmaFilter, AliFemtoV0TrackCutNSigmaFilter, AliFemtoXiTrackCut, AliFemtoV0PairCut,
 51 AliFemtoV0TrackPairCut, AliFemtoXiTrackPairCut, and AliFemtoAnalysisLambdaKaon. All of these
 52 classes are contained in /AliPhysics/PWGCF/FEMTOSCOPY/AliFemto and .../AliFemtoUser.

53 **3 Data Selection**

54 **3.1 Event Selection and Mixing**

55 The events used in this study were selected with the class AliFemtoEventCutEstimators according to the
 56 following criteria:

- 57 – Triggers
 - 58 – minimum bias (kMB)
 - 59 – central (kCentral)
 - 60 – semi-central (kSemiCentral)
- 61 – z-position of reconstructed event vertex must be within 10 cm of the center of the ALICE detector
- 62 – the event must contain at least one particle of each type from the pair of interest

63 The event mixing was handled by the AliFemtoVertexMultAnalysis class, which only mixes events with
 64 like vertex position and centrality. The following criteria were used for event mixing:

- 65 – Number of events to mix = 5
- 66 – Vertex position bin width = 2 cm
- 67 – Centrality bin width = 5

68 The AliFemtoEventReaderAODChain class is used to read the events. Event flattening is not currently
 69 used. FilterBit(7). The centrality is determined by the “V0M” method of AliCentrality, set by calling Al-
 70 iFemtoEventReaderAOD::SetUseMultiplicity(kCentrality). I utilize the SetPrimaryVertexCorrectionT-
 71 PCPoints switch, which causes the reader to shift all TPC points to be relative to the event vertex.

72 **3.2 K^\pm Track Selection**

73 Charged kaons are identified using the AliFemtoESDTrackCutNSigmaFilter class. The specific cuts used
 74 in this analysis are as follows:

75 Track Selection:

- 76 – Kinematic range:
 - 77 – $0.14 < p_T < 1.5$
 - 78 – $|\eta| < 0.8$
- 79 – FilterBit(7)
 - 80 – TPC tracks
- 81 – Track Quality
 - 82 – Minimum number of clusters in the TPC (fminTPCncls) = 80
 - 83 – Maximum allowed χ^2/N_{DOF} for ITS clusters = 3.0
 - 84 – Maximum allowed χ^2/N_{DOF} for TPC clusters = 4.0
- 85 – Primary Particle Selection:

- 86 – Maximum XY impact parameter = 2.4
- 87 – Maximum Z impact parameter = 3.0
- 88 – Remove particles with any kink labels (fRemoveKinks = true)
- 89 – Maximum allowed sigma to primary vertex (fMaxSigmaToVertex) = 3.0

90 K $^\pm$ Identification:

- 91 – PID Probabilities:

- 92 – K: > 0.2
- 93 – π : < 0.1
- 94 – μ : < 0.8
- 95 – p: < 0.1

- 96 – Most probable particle type must be Kaon (fMostProbable=3)

- 97 – TPC and TOF N $_\sigma$ cuts:

- 98 – p < 0.4 GeV/c: N $_{\sigma K,TPC}$ < 2
- 99 – 0.4 < p < 0.45 GeV/c: N $_{\sigma K,TPC}$ < 1
- 100 – 0.45 < p < 0.8 GeV/c: N $_{\sigma K,TPC}$ < 3 & N $_{\sigma K,TOF}$ < 2
- 101 – 0.8 < p < 1.0 GeV/c: N $_{\sigma K,TPC}$ < 3 & N $_{\sigma K,TOF}$ < 1.5
- 102 – p > 1.0 GeV/c: N $_{\sigma K,TPC}$ < 3 & N $_{\sigma K,TOF}$ < 1

- 103 – Electron Rejection: Reject if N $_{\sigma e-,TPC}$ < 3

- 104 – Pion Rejection: Reject if:

- 105 – p < 0.65
 - 106 * if TOF and TPC available: N $_{\sigma \pi,TPC}$ < 3 & N $_{\sigma \pi,TOF}$ < 3
 - 107 * else
 - 108 · p < 0.5: N $_{\sigma \pi,TPC}$ < 3
 - 109 · 0.5 < p < 0.65: N $_{\sigma \pi,TPC}$ < 2
- 110 – 0.65 < p < 1.5: N $_{\sigma \pi,TPC}$ < 5 & N $_{\sigma \pi,TOF}$ < 3
- 111 – p > 1.5: N $_{\sigma \pi,TPC}$ < 5 & N $_{\sigma \pi,TOF}$ < 2

112 The purity of the K $^\pm$ collections was estimated using the MC data, for which the true identity of each
 113 reconstructed K $^\pm$ particle is known. Therefore, the purity may be estimated as:

$$\text{Purity}(K^\pm) = \frac{N_{\text{true}}}{N_{\text{reconstructed}}} \quad (1)$$

114 Purity(K $^+$) \approx Purity(K $^-$) \approx 97%

115 **3.3 V0 Selection**

116 Λ ($\bar{\Lambda}$) and K_S^0 are neutral particles which cannot be directly detected, but must instead be reconstructed
 117 through detection of their decay products, or daughters. This process is illustrated in Figure 1. In
 118 general, particles which are topologically reconstructed in this fashion are called V0 particles. The
 119 class AliFemtoV0TrackCutNSigmaFilter (which is an extension of AliFemtoV0TrackCut) is used to
 120 reconstruct the V0s.

121 In order to obtain a true and reliable signal, one must ensure good purity of the V0 collection. The purity
 122 of the collection is calculated as:

$$\text{Purity} = \frac{\text{Signal}}{\text{Signal} + \text{Background}} \quad (2)$$

123 To obtain both the signal and background, the invariant mass distribution (m_{inv}) of all V0 candidates
 124 must be constructed immediately before the final invariant mass cut. Examples of such distributions can
 125 be found in Figures 3 and 5. It is vital that this distribution be constructed immediately before the final
 126 m_{inv} cut, otherwise it would be impossible to estimate the background. As shown in Figures 3 and 5, the
 127 background is fit (with a polynomial) outside of the peak region of interest to obtain an estimate for the
 128 background within the region. Within the m_{inv} cut limits, the background is the region below the fit while
 129 the signal is the region above the fit.

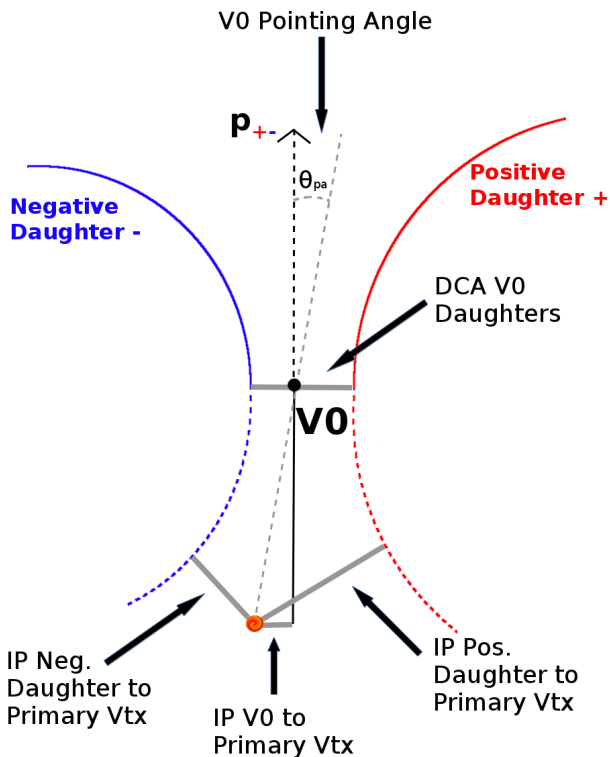


Fig. 1: V0 Reconstruction

130 **3.3.1 Λ Reconstruction**

131 The following cuts were used to select good Λ ($\bar{\Lambda}$) candidates:

- 132 1. Daughter Particle Cuts

- 133 (a) Cuts Common to Both Daughters
- 134 i. $|\eta| < 0.8$
- 135 ii. SetTPCnclsDaughters(80)
- 136 iii. SetStatusDaughters(AliESDtrack::kTPCrefic)
- 137 iv. SetMaxDcaV0Daughters(0.4)
- 138 (b) Pion Specific Daughter Cuts
- 139 i. $p_T > 0.16$
- 140 ii. DCA to prim vertex > 0.3
- 141 (c) Proton Specific Daughter Cuts
- 142 i. $p_T > 0.5(p) [0.3(\bar{p})] \text{ GeV}/c$
- 143 ii. DCA to prim vertex > 0.1

144 2. V0 Cuts

- 145 (a) $|\eta| < 0.8$
- 146 (b) $p_T > 0.4$
- 147 (c) $|m_{inv} - m_{PDG}| < 3.8 \text{ MeV}$
- 148 (d) DCA to prim. vertex $< 0.5 \text{ cm}$
- 149 (e) Cosine of pointing angle > 0.9993
- 150 (f) OnFlyStatus = false
- 151 (g) Decay Length $< 60 \text{ cm}$

152 3. Shared Daughter Cut for V0 Collection

- 153 – Iterate through V0 collection to ensure that no daughter is used in more than one V0 candidate

154 Figure 2a shows the mass assuming K_S^0 hypothesis for the Λ collection, i.e. assume the daughters are
 155 $\pi^+\pi^-$ instead of $\pi^+\bar{p}^-$. Figure 2b is a similar plot, but is for the $\bar{\Lambda}$ collection, i.e. assume the daughters
 156 are $\pi^+\pi^-$ instead of $\pi^+\bar{p}^-$. The K_S^0 contamination is visible, although not profound, in both in the slight
 157 peaks around $m_{inv} = 0.497 \text{ GeV}/c^2$. If one simply cuts out the entire peak, good Λ particles will be
 158 lost. Ideally, the Λ selection and K_S^0 misidentification cuts are selected such that the peak is removed
 159 from this plot while leaving the distribution continuous. To attempt to remove these K_S^0 contaminations
 160 without throwing away good Λ and $\bar{\Lambda}$ particles, the following misidentification cuts are imposed; a $\Lambda(\bar{\Lambda})$
 161 candidate is rejected if all of the following criteria are satisfied:

- 162 – $|m_{inv, K_S^0 \text{ Hypothesis}} - m_{PDG, K_S^0}| < 9.0 \text{ MeV}/c^2$
- 163 – Positive and negative daughters pass π daughter cut implemented for K_S^0 reconstruction
- 164 – $|m_{inv, K_S^0 \text{ Hypothesis}} - m_{PDG, K_S^0}| < |m_{inv, \Lambda(\bar{\Lambda}) \text{ Hypothesis}} - m_{PDG, \Lambda(\bar{\Lambda})}|$

165 Figure 3 shows the invariant mass (M_{inv}) distribution of all $\Lambda(\bar{\Lambda})$ candidates immediately before the final
 166 invariant mass cut. These distributions are used to calculate the collection purities. The Λ and $\bar{\Lambda}$ purities
 167 are found to be: $\text{Purity}(\Lambda) \approx \text{Purity}(\bar{\Lambda}) \approx 95\%$.

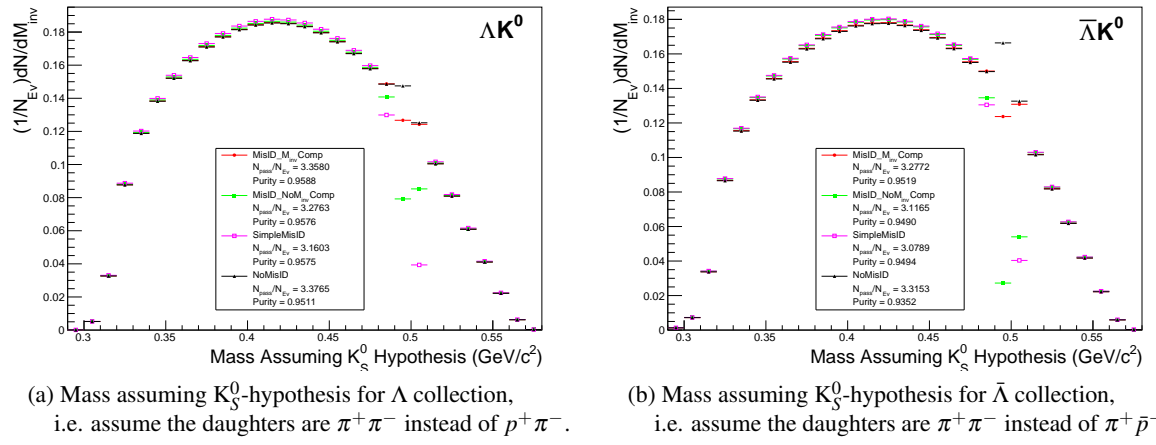


Fig. 2: Mass assuming K_S^0 -hypothesis for V0 candidates passing all Λ (2a) and $\bar{\Lambda}$ (2b) cuts. The “NoMisID” distribution (black triangles) uses the V0 finder without any attempt to remove misidentified K_S^0 . The slight peak in the “NoMisID” distribution around $m_{inv} = 0.5$ GeV/c² contains misidentified K_S^0 particles in our $\Lambda(\bar{\Lambda})$ collection. “SimpleMisID” (pink squares) simply cuts out the entire peak, which throws away some good Λ and $\bar{\Lambda}$ particles. “MisID_NoM_{inv}Comp” (green squares) uses the misidentification cut outlined in the text, but does not utilize the invariant mass comparison method. “MisID_M_{inv}Comp” (red circles) utilizes the full misidentification methods, and is currently used for this analysis. “N_{pass}/N_{ev}” is the total number of $\Lambda(\bar{\Lambda})$ particles found, normalized by the total number of events. The purity of the collection is also listed.

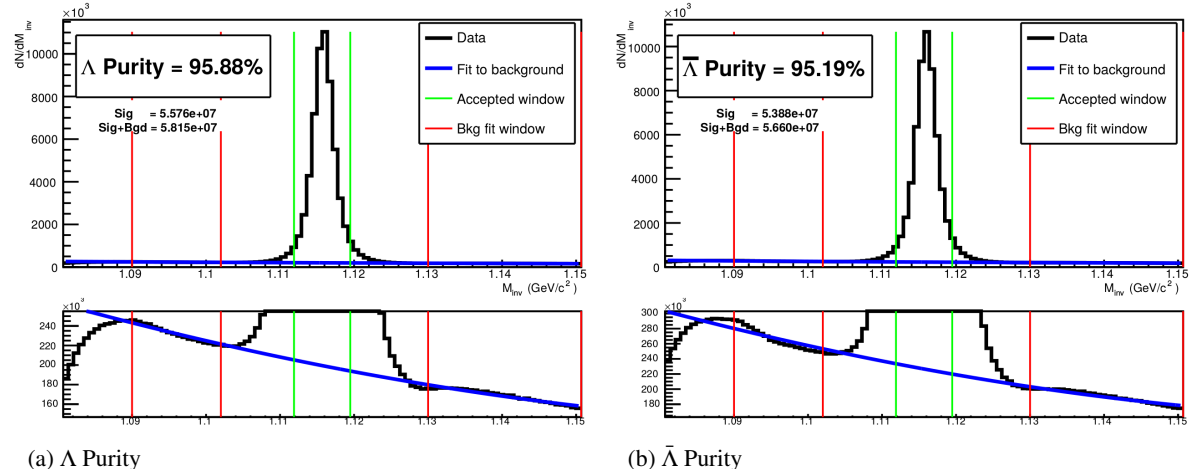


Fig. 3: Invariant mass (M_{inv}) distribution of all Λ (a) and $\bar{\Lambda}$ (b) candidates immediately before the final invariant mass cut. The bottom figures are zoomed to show the background with fit. The vertical green lines represent the M_{inv} cuts used in the analyses, the red vertical lines delineate the region over which the background was fit, and the blue line shows the background fit. These distributions are used to calculate the collection purities, Purity(Λ) \approx Purity($\bar{\Lambda}$) \approx 95%.

168 3.3.2 K_S^0 Reconstruction

169 The following cuts were used to select good K_S^0 candidates:

170 1. Pion Daughter Cuts

- 171 (a) $|\eta| < 0.8$
- 172 (b) SetTPCnclsDaughters(80)

- 173 (c) SetStatusDaughters(AliESDtrack::kTPCrefic)
- 174 (d) SetMaxDcaV0Daughters(0.3)
- 175 (e) $p_T > 0.15$
- 176 (f) DCA to prim vertex > 0.3

177 2. K_S^0 Cuts

- 178 (a) $|\eta| < 0.8$
- 179 (b) $p_T > 0.2$
- 180 (c) $m_{PDG} - 13.677 \text{ MeV} < m_{inv} < m_{PDG} + 2.0323 \text{ MeV}$
- 181 (d) DCA to prim. vertex $< 0.3 \text{ cm}$
- 182 (e) Cosine of pointing angle > 0.9993
- 183 (f) OnFlyStatus = false
- 184 (g) Decay Length $< 30 \text{ cm}$

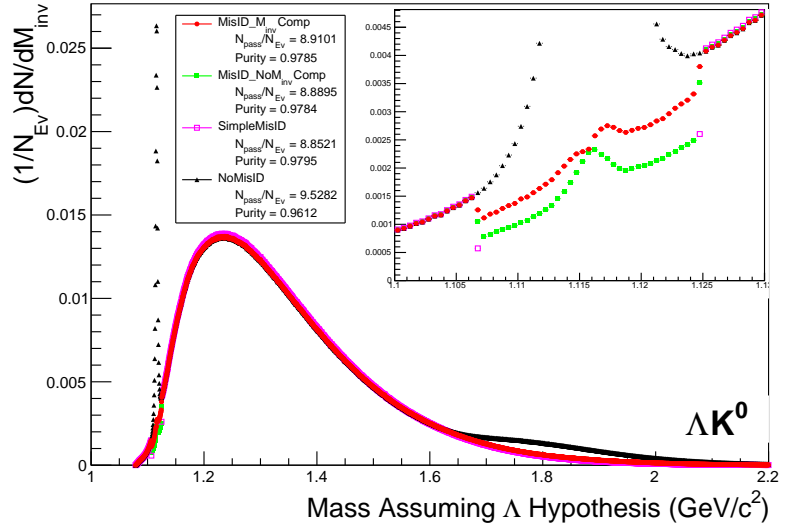
185 3. Shared Daughter Cut for V0 Collection

- 186 – Iterate through V0 collection to ensure that no daughter is used in more than one V0 candidate

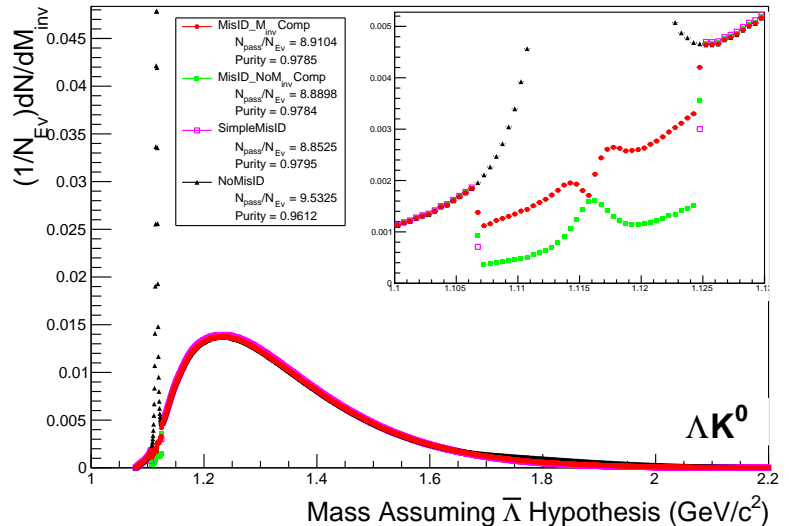
187 As can be seen in Figure 4, some misidentified Λ and $\bar{\Lambda}$ particles contaminate our K_S^0 sample. Figure
 188 4a shows the mass assuming Λ -hypothesis for the K_S^0 collection, i.e. assume the daughters are $p^+\pi^-$
 189 instead of $\pi^+\pi^-$. Figure 4b is similar, but shows the mass assuming $\bar{\Lambda}$ hypothesis for the collection,
 190 i.e. assume the daughters are $\pi^+\bar{p}^-$ instead of $\pi^+\pi^-$. The Λ contamination can be seen in 4a, and the
 191 $\bar{\Lambda}$ contamination in 4b, in the peaks around $m_{inv} = 1.115 \text{ GeV}/c^2$. Additionally, the $\bar{\Lambda}$ contamination is
 192 visible in Figure 4a, and the Λ contamination visible in Figure 4b, in the region of excess around 1.65
 193 $< m_{inv} < 2.1 \text{ GeV}/c^2$. This is confirmed as the number of misidentified Λ particles in the sharp peak
 194 of Figure 4a (misidentified $\bar{\Lambda}$ particles in the sharp peak of Figure 4b) approximately equals the excess
 195 found in the $1.65 < m_{inv} < 2.1 \text{ GeV}/c^2$ region of Figure 4a (Figure 4b).

196 The peaks around $m_{inv} = 1.115 \text{ GeV}/c^2$ in Figure 4 contain both misidentified Λ ($\bar{\Lambda}$) particles and good
 197 K_S^0 . If one simply cuts out the entire peak, some good K_S^0 particles will be lost. Ideally, the K_S^0 selection
 198 and $\Lambda(\bar{\Lambda})$ misidentification cuts can be selected such that the peak is removed from this plot while leaving
 199 the distribution continuous. To attempt to remove these Λ and $\bar{\Lambda}$ contaminations without throwing away
 200 good K_S^0 particles, the following misidentification cuts are imposed; a K_S^0 candidate is rejected if all of
 201 the following criteria are satisfied (for either Λ or $\bar{\Lambda}$ hypothesis):

- 202 – $|m_{inv, \Lambda(\bar{\Lambda}) \text{ Hypothesis}} - m_{PDG, \Lambda(\bar{\Lambda})}| < 9.0 \text{ MeV}/c^2$
- 203 – Positive daughter passes $p^+(\pi^+)$ daughter cut implemented for $\Lambda(\bar{\Lambda})$ reconstruction
- 204 – Negative daughter passes $\pi^-(\bar{p}^-)$ daughter cut implemented by $\Lambda(\bar{\Lambda})$ reconstruction
- 205 – $|m_{inv, \Lambda(\bar{\Lambda}) \text{ Hypothesis}} - m_{PDG, \Lambda(\bar{\Lambda})}| < |m_{inv, K_S^0 \text{ Hypothesis}} - m_{PDG, K_S^0}|$



(a) Mass assuming Λ -hypothesis for K_S^0 collection, i.e. assume the daughters are $p^+ \pi^-$ instead of $\pi^+ \pi^-$.



(b) Mass assuming $\bar{\Lambda}$ -hypothesis for K_S^0 collection, i.e. assume the daughters are $\pi^+ \bar{p}^-$ instead of $\pi^+ \pi^-$.

Fig. 4: Mass assuming Λ -hypothesis (4a) and $\bar{\Lambda}$ -hypothesis (4b) for K_S^0 collection. The “NoMisID” distribution (black triangles) uses the V0 finder without any attempt to remove misidentified Λ and $\bar{\Lambda}$. The peak in the “NoMisID” distribution around $m_{\text{inv}} = 1.115 \text{ GeV}/c^2$ contains misidentified Λ (4a) and $\bar{\Lambda}$ (4b) particles in our K_S^0 collection. “SimpleMisID” (pink squares) simply cuts out the entire peak, which throws away some good K_S^0 particles. “MisID_NoM_{inv}Comp” (green squares) uses the misidentification cut outlined in the text, but does not utilize the invariant mass comparison method. “MisID_M_{inv}Comp” (red circles) utilizes the full misidentification methods, and is currently used for this analysis. “ $N_{\text{pass}}/N_{\text{ev}}$ ” is the total number of K_S^0 particles found, normalized by the total number of events. The purity of the collection is also listed. Also note, the relative excess of the “NoMisID” distribution around $1.65 < m_{\text{inv}} < 2.1 \text{ GeV}/c^2$ shows misidentified $\bar{\Lambda}$ (4a) and Λ (4b) particles in our K_S^0 collection.

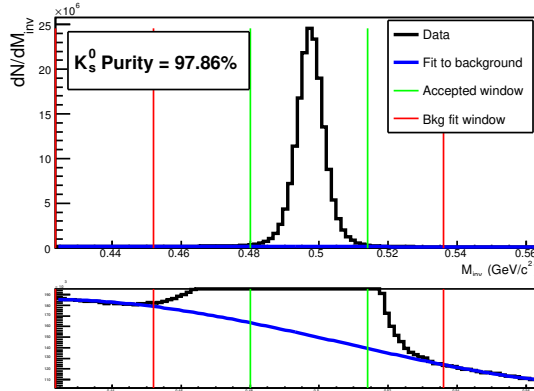


Fig. 5: Invariant mass (M_{inv}) distribution of all K_s^0 candidates immediately before the final invariant mass cut. The bottom figure is zoomed to show the background with fit. The vertical green lines represent the M_{inv} cut used in the analyses, the red vertical lines delineate the region over which the background was fit, and the blue line shows the background fit. This distribution is used to calculate the collection purity, $Purity(K_s^0) \approx 98\%$.

206 3.4 Cascade Reconstruction

207 Our motivation for studying ΞK^\pm systems is to hopefully better understand the striking difference in the
208 ΛK^+ and ΛK^- data at low k^* (Figure 14).

209 The reconstruction of Ξ particles is one step above V0 reconstruction. V0 particles are topologically
210 reconstructed by searching for the charged daughters' tracks into which they decay. With Ξ particles, we
211 search for the V0 particle and charged daughter into which the Ξ decays. In the case of Ξ^- , we search
212 for the Λ (V0) and π^- (track) daughters. We will refer to this π as the “bachelor π ”.

213 The following cuts were used to select good Ξ^- ($\bar{\Xi}^+$) candidates:

214 1. V0 Daughter Reconstruction

215 (a) V0 Daughter Particle Cuts

216 i. Cuts Common to Both Daughters

- 217 A. $|\eta| < 0.8$
- 218 B. SetTPCnclsDaughters(80)
- 219 C. SetStatusDaughters(AliESDtrack::kTPCrefic)
- 220 D. SetMaxDcaV0Daughters(0.4)

221 ii. Pion Specific Daughter Cuts

- 222 A. $p_T > 0.16$
- 223 B. DCA to prim vertex > 0.3
- 224 iii. Proton Specific Daughter Cuts
- 225 A. $p_T > 0.5(p) [0.3(\bar{p})]$ GeV/ c
- 226 B. DCA to prim vertex > 0.1

227 (b) V0 Cuts

- 228 i. $|\eta| < 0.8$
- 229 ii. $p_T > 0.4$ GeV/ c
- 230 iii. $|m_{inv} - m_{PDG}| < 3.8$ MeV
- 231 iv. DCA to prim. vertex > 0.2 cm
- 232 v. Cosine of pointing angle to Ξ decay vertex > 0.9993

233 vi. OnFlyStatus = false
 234 vii. Decay Length < 60 cm
 235 viii. The misidentification cuts described in Section 3.3.1 are utilized
 236 2. Bachelor π Cuts
 237 (a) $|\eta| < 0.8$
 238 (b) $p_T < 100 \text{ GeV}/c$
 239 (c) DCA to prim vertex > 0.1 cm
 240 (d) SetTPCnclsDaughters(70)
 241 (e) SetStatusDaughters(AliESDtrack::kTPCrefic)
 242 3. Ξ Cuts
 243 (a) $|\eta| < 0.8$
 244 (b) $0.8 < p_T < 100 \text{ GeV}/c$
 245 (c) $|m_{inv} - m_{PDG}| < 3.0 \text{ MeV}$
 246 (d) DCA to prim. vertex < 0.3 cm
 247 (e) Cosine of pointing angle > 0.9992
 248 4. Shared Daughter Cut for Ξ Collection
 249 – Iterate through Ξ collection to ensure that no daughter is used in more than one Ξ candidate

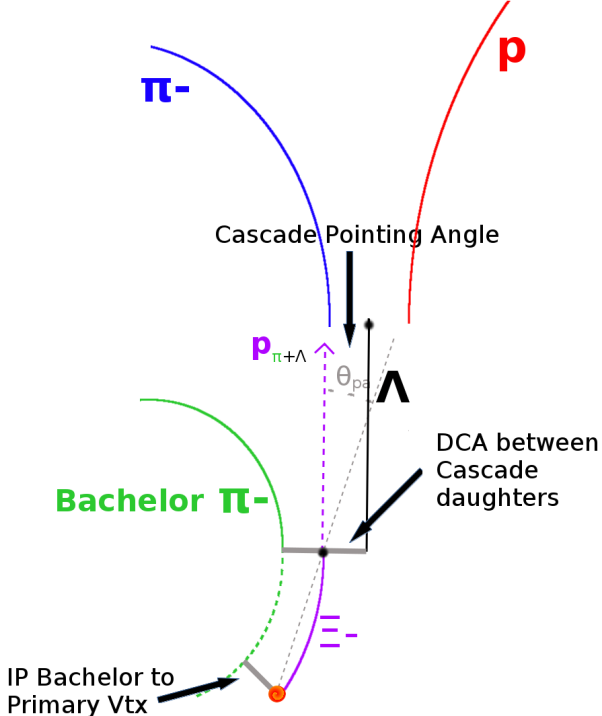


Fig. 6: Ξ Reconstruction

250 The purity of our Ξ and $\bar{\Xi}$ collections are calculated just as those of our V0 collections 3.3. Figure 7,
 251 which is used to calculate the purity, shows the m_{inv} distribution of our $\Xi(\bar{\Xi})$ candidates just before the
 252 final m_{inv} cut. Currently, we have Purity(Ξ^-) $\approx 90\%$ and Purity($\bar{\Xi}^+$) $\approx 92\%$.

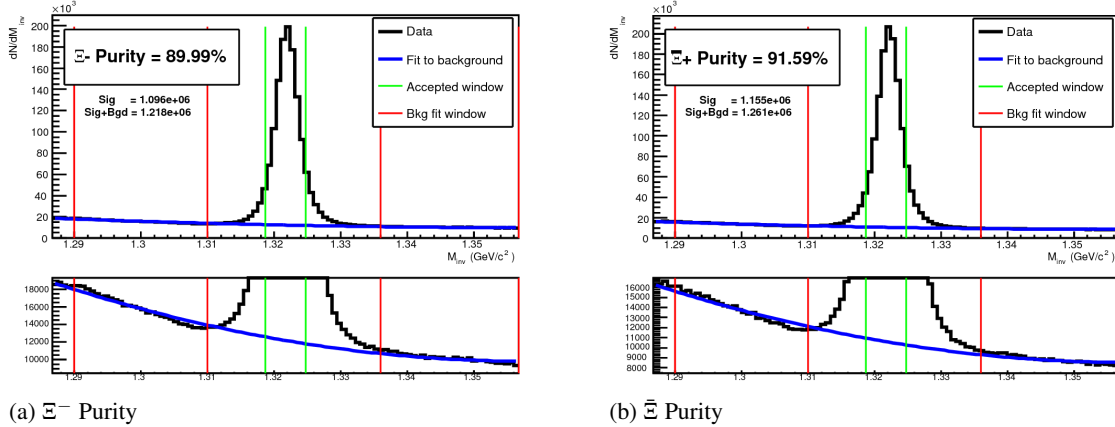


Fig. 7: Ξ^- ($\bar{\Xi}^+$) Purity 0-10%: Purity(Ξ^-) \approx 90% and Purity($\bar{\Xi}^+$) \approx 92%.

253 3.5 Pair Selection

254 It is important to obtain true particle pairs in the analysis. In particular, contamination from pairs con-
 255 structed with split or merged tracks, and pairs sharing daughters, can introduce an artificial signal into
 256 the correlation function, obscuring the actual physics.

257 1. Shared Daughter Cut for Pairs

258 (a) V0-V0 Pairs (i.e. $\Lambda(\bar{\Lambda})K_S^0$ analyses)

- 259 – Remove all pairs which share a daughter
- 260 – Ex. Λ and K_S^0 particles which share a π^- daughter are not included

261 (b) V0-Track Pairs (i.e. $\Lambda(\bar{\Lambda})K^\pm$ analyses)

- 262 – Remove pairs if Track is also used as a daughter of the V0
- 263 – In these analyses, this could only occur if, for instance, a K is misidentified as a π
- 264 – or p in the V0 reconstruction

265 (c) Ξ -Track Pairs

- 266 – Remove pairs if Track is also used as a daughter of the Ξ
- 267 – In these analyses, this could only occur if, for instance, a K is misidentified as a π
- 268 – or p in the V0 reconstruction, or misidentified as bachelor π .
- 269 – Remove pair if bachelor π is also a daughter of the Λ
- 270 – This is not a pair cut, but is included here because this cut occurs in the
- 271 – AliFemtoXiTrackPairCut class

272 2. Average Separation Cuts

- 273 – Used to cut out splitting and merging effects
- 274 – The motivation for these cuts can be seen in Figures 8, 9, and 10, in which average separation
- 275 – correlation functions are presented

276 (a) $\Lambda(\bar{\Lambda})K_S^0$ Analyses

- 277 – Average separation > 6.0 cm for like charge sign daughters
- 278 – ex. p daughter of Λ and π^+ daughter of K_S^0
- 279 – No cut for unlike-sign daughters

280 (b) $\Lambda(\bar{\Lambda})K^\pm$ Analyses

- 281 – Average Separation > 8.0 cm for daughter of $\Lambda(\bar{\Lambda})$ sharing charge sign of K^\pm
 282 – ex. in ΛK^+ analysis, p daughter of Λ with K^+
 283 – No cut for unlike signs

284 (c) $\Xi(\bar{\Xi})K^\pm$ Analyses

- 285 – Average Separation > 8.0 cm for any daughter of Ξ sharing charge sign of K^\pm
 286 – ex. in $\Xi^- K^-$ analysis, π^- daughter of Λ daughter with K^- , and bachelor π^- daugh-
 287 ter with K^-
 288 – No cut for unlike signs

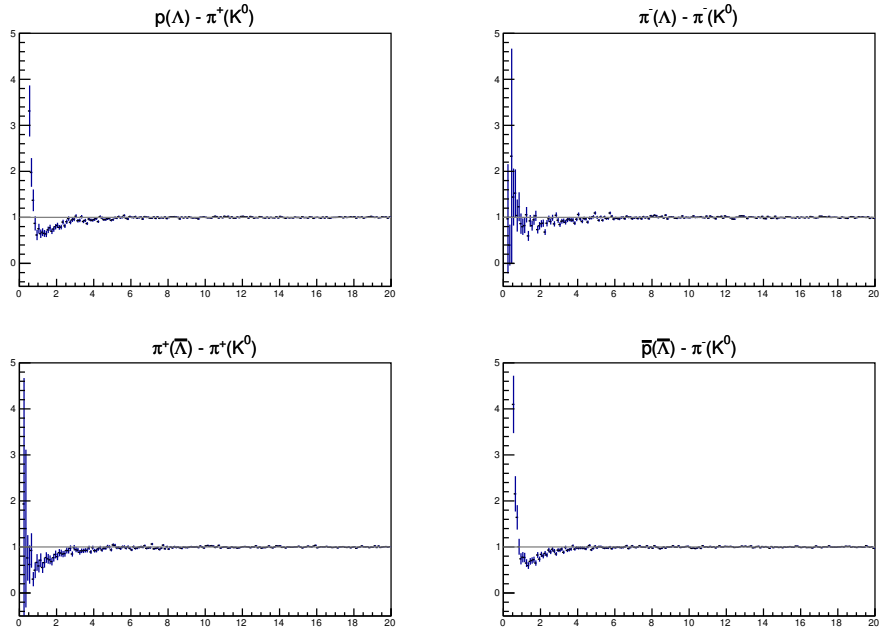


Fig. 8: Average separation (cm) correlation functions of $\Lambda(\bar{\Lambda})$ and K_S^0 Daughters. Only like-sign daughter pairs are shown (the distributions for unlike-signs were found to be flat). The title of each subfigure shows the daughter pair, as well as the mother of each daughter (in “()”), ex. top left is p from Λ with π^+ from K_S^0 .

289 **4 Correlation Functions**

290 This analysis studies the momentum correlations of both Λ -K and Ξ -K pairs using the two-particle cor-
 291 relation function, defined as $C(k^*) = A(k^*)/B(k^*)$, where $A(k^*)$ is the signal distribution, $B(k^*)$ is the
 292 reference (or background) distribution, and k^* is the momentum of one of the particles in the pair rest
 293 frame. In practice, $A(k^*)$ is constructed by binning in k^* pairs from the same event. Ideally, $B(k^*)$ is sim-
 294 ilar to $A(k^*)$ in all respects excluding the presence of femtoscopic correlations [2]; as such, $B(k^*)$ is used
 295 to divide out the phase-space effects, leaving only the femtoscopic effects in the correlation function.

296 In practice, $B(k^*)$ is obtained by forming mixed-event pairs, i.e. particles from a given event are paired
 297 with particles from $N_{mix}(= 5)$ other events, and these pairs are then binned in k^* . In forming the back-
 298 ground distribution, it is important to mix only similar events; mixing events with different phase-spaces
 299 can lead to artificial signals in the correlation function. Therefore, in this analysis, we mix events with
 300 primary vertices within 2 cm and centralities within 5% of each other. Also note, a vertex correction is
 301 also applied to each event, which essentially re-centers the primary vertices to $z = 0$.

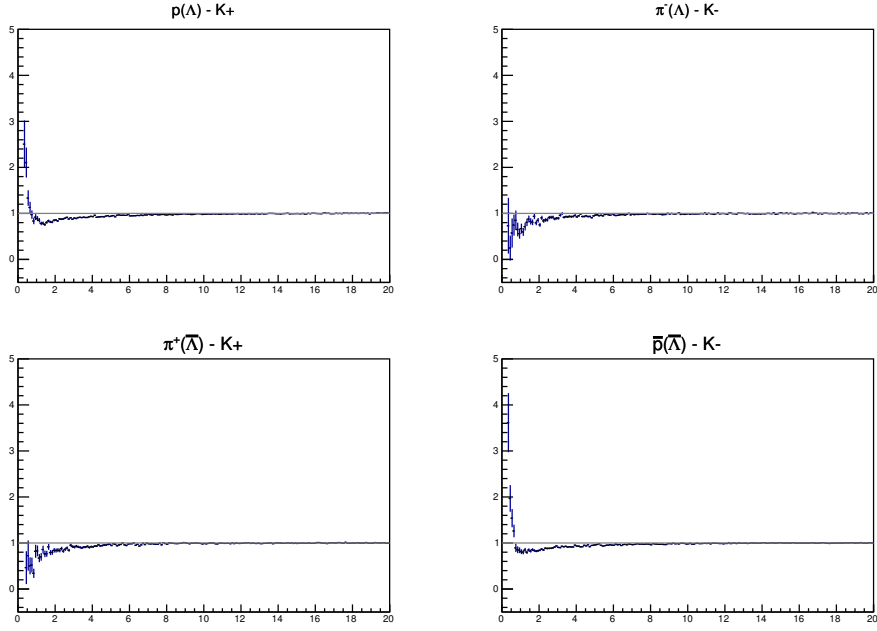


Fig. 9: Average separation (cm) correlation functions of $\Lambda(\bar{\Lambda})$ Daughter and K^\pm . Only like-sign pairs are shown (unlike-signs were flat). In the subfigure titles, the particles in “()” represent the mothers, ex. top left is p from Λ with K^+ .

302 This analysis presents correlation functions for three centrality bins (0-10%, 10-30%, and 30-50%),
 303 and is currently pair transverse momentum ($k_T = 0.5|\mathbf{p}_{T,1} + \mathbf{p}_{T,2}|$) integrated (i.e. not binned in k_T).
 304 The correlation functions are constructed separately for the two magnetic field configurations, and are
 305 combined using a weighted average:

$$C_{combined}(k^*) = \frac{\sum_i w_i C_i(k^*)}{\sum_i w_i} \quad (3)$$

306 where the sum runs over the correlation functions to be combined, and the weight, w_i , is the number of
 307 numerator pairs in $C_i(k^*)$. Here, the sum is over the two field configurations.

308 Figures 11, 12, and 13 show the correlation functions for all centralities studied for $\Lambda K_S^0(\bar{\Lambda} K_S^0)$, $\Lambda K^+(\bar{\Lambda} K^-)$,
 309 and $\Lambda K^-(\bar{\Lambda} K^+)$, respectively. All were normalized in the range $0.32 < k^* < 0.4$ GeV/c.

310 5 Fitting

311 5.1 Model: ΛK_S^0 , ΛK^\pm , $\Xi^{ch} K_S^0$

312 In the absence of Coulomb effects, and assuming a spherically gaussian source of width R , the 1D
 313 femtoscopic correlation function can be calculated analytically using:

$$C(k^*) = 1 + \lambda [C_{QI}(k^*) + C_{FSI}(k^*)] \quad (4)$$

314 C_{QI} describes plane-wave quantum interference:

$$C_{QI}(k^*) = \alpha \exp(-4k^{*2}R^2) \quad (5)$$

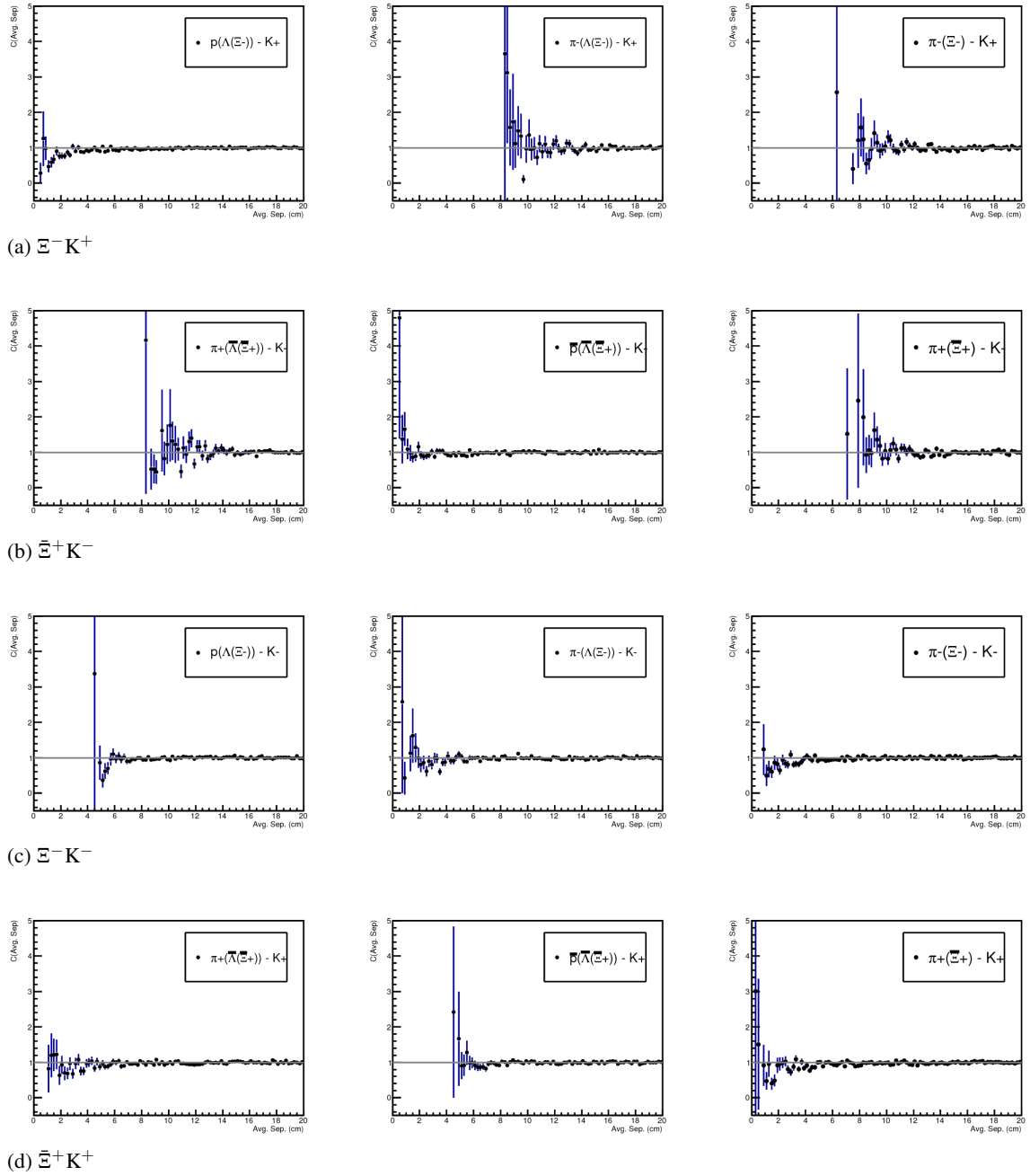


Fig. 10: Average separation (cm) correlation functions of Ξ Daughter and K^\pm . In the subfigure titles, the particles in “()” represent the mothers, ex. top left is p from Λ from Ξ^- with K^+ .

where $\alpha = (-1)^{2j}/(2j+1)$ for identical particles with spin j , and $\alpha = 0$ for non-identical particles. Obviously, $\alpha = 0$ for all analyses presented in this note. C_{FSI} describes the s-wave strong final state interaction between the particles:

$$C_{FSI}(k^*) = (1 + \alpha) \left[\frac{1}{2} \left| \frac{f(k^*)}{R} \right|^2 \left(1 - \frac{d_0}{2\sqrt{\pi R}} \right) + \frac{2\mathbb{R}f(k^*)}{\sqrt{\pi R}} F_1(2k^*R) - \frac{\mathbb{I}f(k^*)}{R} F_2(2k^*R) \right]$$

$$f(k^*) = \left(\frac{1}{f_0} + \frac{1}{2} d_0 k^{*2} - ik^* \right)^{-1}; \quad F_1(z) = \int_0^z \frac{e^x - z^2}{z} dx; \quad F_2(z) = \frac{1 - e^{-z^2}}{z} \quad (6)$$

where R is the source size, $f(k^*)$ is the s-wave scattering amplitude, f_0 is the complex scattering length,

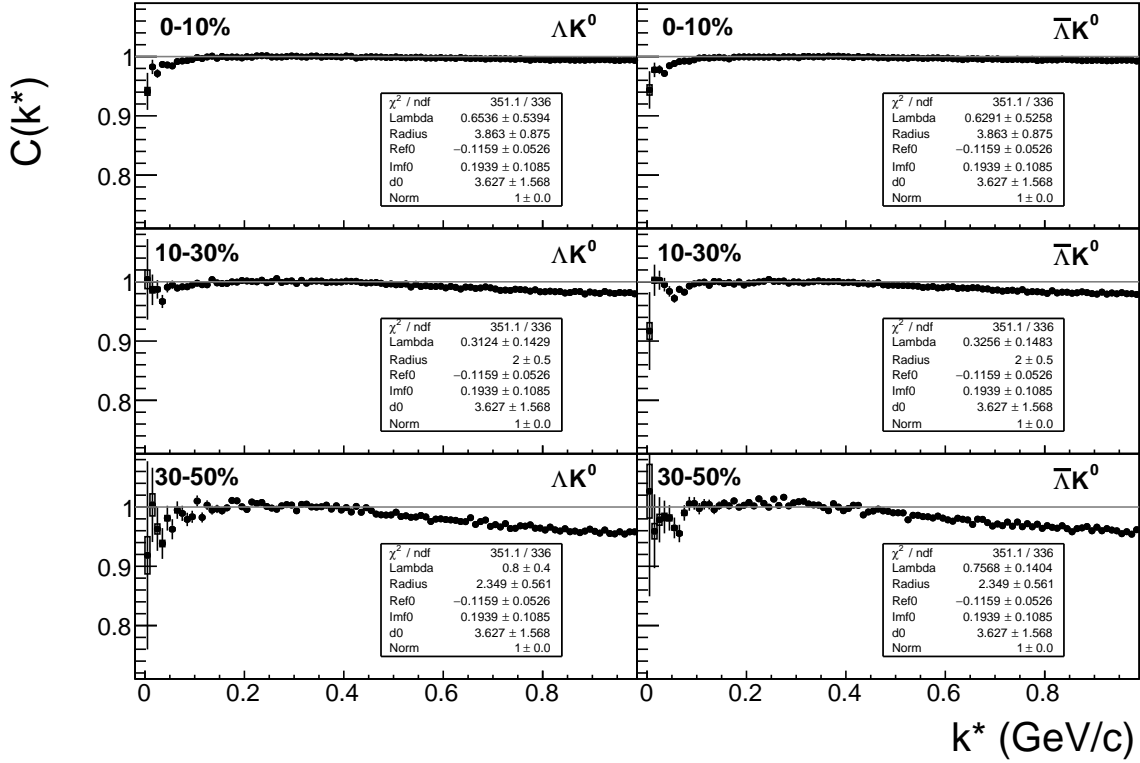


Fig. 11: ΛK_S^0 (left) and $\bar{\Lambda} K_S^0$ (right) correlation functions for 0-10% (top), 10-30% (middle), and 30-50% (bottom) centralities. The lines represent the statistical errors, while the boxes represent the systematic errors.

and d_0 is the effective range of the interaction.

The code developed to fit the data is called “LednickyFitter”, and utilizes the ROOT TMinuit implementation of the MINUIT fitting package. In short, given a function with a number of parameters, the fitter explores the parameter space searching for the minimum of the equation. In this implementation, the function to be minimized should represent the difference between the measure and theoretical correlation functions. However, a simple χ^2 test is inappropriate for fitting correlation functions, as the ratio two Poisson distributions does not result in a Poisson distribution. Instead, a log-likelihood fit function of the following form is used [2]:

$$\chi_{PML}^2 = -2 \left[A \ln \left(\frac{C(A+B)}{A(C+1)} \right) + B \ln \left(\frac{A+B}{B(C+1)} \right) \right] \quad (7)$$

where A is the experimental signal distribution (numerator), B is the experimental background distribution (denominator), and C is the theoretical fit correlation function.

The LednickyFitter uses Equations 4 – 6 to build the theoretical fit, and Equation 7 as the statistic quantifying the quality of the fit. The parameters to be varied by MINUIT are: λ , R , f_0 ($\mathbb{R}f_0$ and $\mathbb{I}f_0$ separately), d_0 , and normalization N . The fitter currently includes methods to correct for momentum resolution and a non-flat background. These corrections are applied to the fit function, the data is never touched. The fitter is able to share parameters between different analyses and fit all simultaneously.

In a typical fit, a given pair is fit with its conjugate (ex. ΛK^+ with $\bar{\Lambda} K^-$) across all centralities (0-10%, 10-30%, 30-50%), for a total of 6 simultaneous analyses. Each analysis has a unique λ and normalization parameter. The radii are shared between analyses of like centrality, as these should have similar source

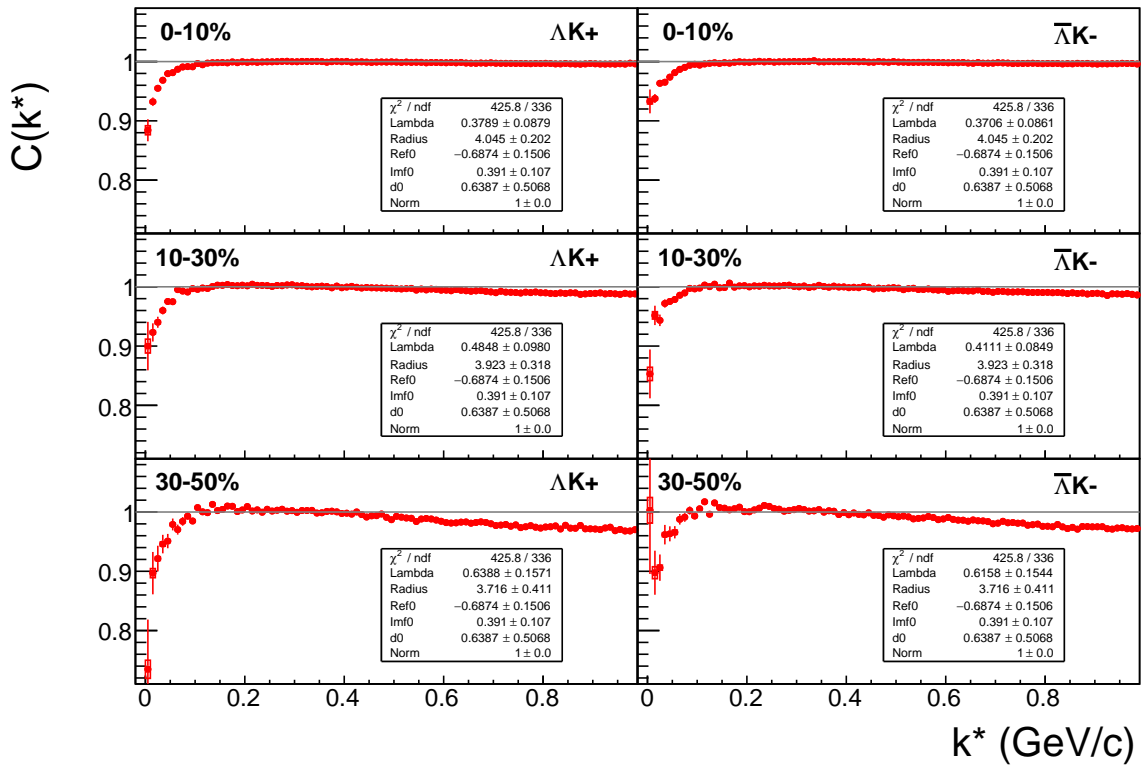


Fig. 12: ΔK^+ (left) and $\bar{\Delta} K^-$ (right) correlation functions for 0-10% (top), 10-30% (middle), and 30-50% (bottom) centralities. The lines represent the statistical errors, while the boxes represent the systematic errors.

337 sizes. The scattering parameters ($\mathbb{R}f_0, \mathbb{I}f_0, d_0$) are shared amongst all.

338 Figures 19, 21, and 23 (Section 7) show experimental data with fits for all studied centralities for ΔK_S^0
 339 with $\bar{\Delta} K_S^0$, ΔK^+ with $\bar{\Delta} K^-$, and ΔK^- with $\bar{\Delta} K^+$, respectively. In the figures, the black solid line
 340 represents the “raw” fit, i.e. not corrected for momentum resolution effects nor non-flat background. The
 341 green line shows the fit to the non-flat background. The purple points show the fit after momentum res-
 342 olution and non-flat background corrections have been applied. The initial values of the parameters is
 343 listed, as well as the final fit values with uncertainties.

344 5.2 Model: $\Xi^{ch} K^{ch}$

345 When fitting the $\Xi^-(\bar{\Xi}^+)K^\pm$ results, it is necessary to include both strong and Coulomb effects. In this
 346 case, Equation 4 is no longer valid, and, in fact, there is no analytical form with which to fit. Therefore,
 347 we must begin with the wave function describing the pair interaction, and simulate many particle pairs
 348 to obtain a theoretical fit correlation function. The code developed to achieve this functionality is called
 349 “CoulombFitter”. Currently, in order to generate the statistics needed for a stable fit, we find that $\sim 10^4$
 350 simulated pairs per 10 MeV bin are necessary. Unfortunately, the nature of this process means that the
 351 “CoulombFitter” takes much longer to run than the “LednickýFitter” of Section 5.1.

352 The two-particle correlation function may be written as:

$$353 C(\mathbf{k}^*) = \sum_S \rho_S \int S(\mathbf{r}^*) |\Psi_{\mathbf{k}^*}^S(\mathbf{r}^*)|^2 d^3 \mathbf{r}^* \quad (8)$$

354 where ρ_S is the normalized emission probability of particles in a state with spin S , $S(\mathbf{r}^*)$ is the pair

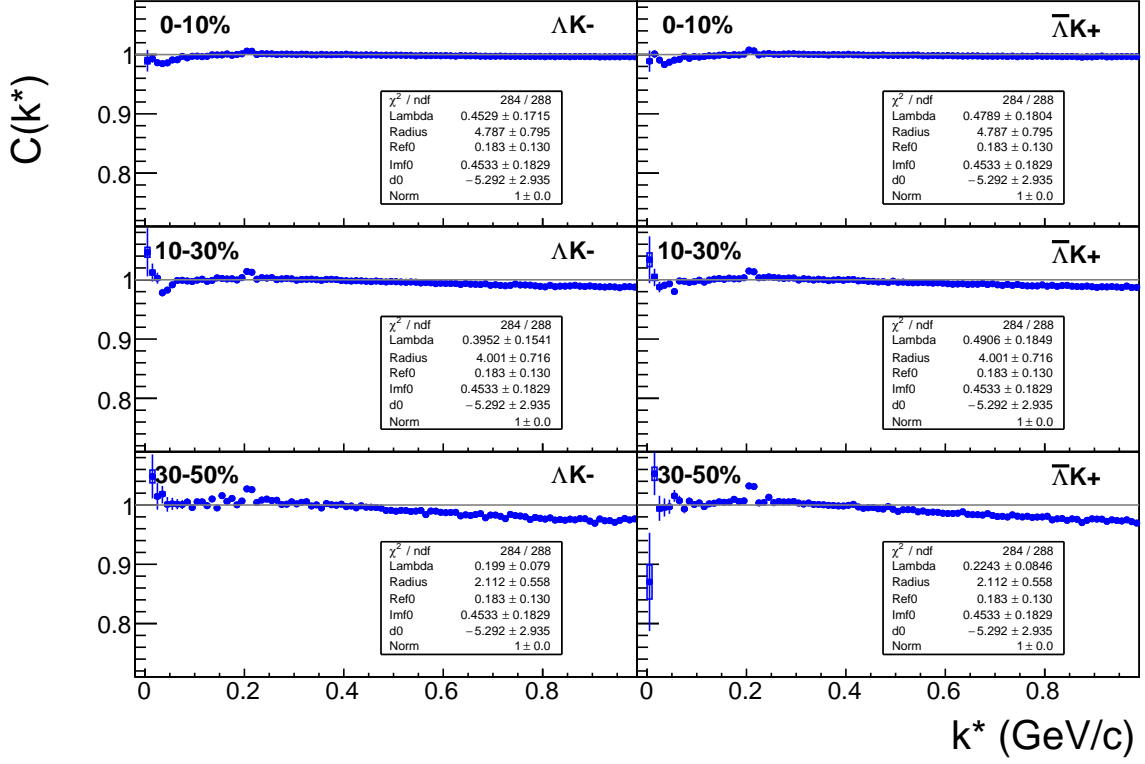


Fig. 13: ΛK^- (left) and $\bar{\Lambda} K^+$ (right) correlation functions for 0-10% (top), 10-30% (middle), and 30-50% (bottom) centralities. The lines represent the statistical errors, while the boxes represent the systematic errors. The peak at $k^* \approx 0.2$ GeV/c is due to the Ω^- resonance.

354 emission source distribution (assumed to be Gaussian), and $\Psi_{\mathbf{k}^*}^S(\mathbf{r}^*)$ is the two-particle wave-function
 355 including both strong and Coulomb interactions [3]:

$$\Psi_{\mathbf{k}^*}(\mathbf{r}^*) = e^{i\delta_c} \sqrt{A_c(\eta)} [e^{i\mathbf{k}^* \cdot \mathbf{r}^*} F(-i\eta, 1, i\xi) + f_c(k^*) \frac{\tilde{G}(\rho, \eta)}{r^*}] \quad (9)$$

356 where $\rho = k^* r^*$, $\eta = (k^* a_c)^{-1}$, $\xi = \mathbf{k}^* \cdot \mathbf{r}^* + k^* r^* \equiv \rho(1 + \cos \theta^*)$, and $a_c = (\mu z_1 z_2 e^2)^{-1}$ is the two-
 357 particle Bohr radius (including the sign of the interaction). δ_c is the Coulomb s-wave phase shift, $A_c(\eta)$
 358 is the Coulomb penetration factor, $\tilde{G} = \sqrt{A_c}(G_0 + iF_0)$ is a combination of the regular (F_0) and singular
 359 (G_0) s-wave Coulomb functions. $f_c(k^*)$ is the s-wave scattering amplitude:

$$f_c(k^*) = [\frac{1}{f_0} + \frac{1}{2} d_0 k^{*2} - \frac{2}{a_c} h(\eta) - ik^* A_c(\eta)]^{-1} \quad (10)$$

360 where, the “h-function”, $h(\eta)$, is expressed through the digamma function, $\psi(z) = \Gamma'(z)/\Gamma(z)$ as:

$$h(\eta) = 0.5[\psi(i\eta) + \psi(-i\eta) - \ln(\eta^2)] \quad (11)$$

361 As stated before, to generate a fit correlation function, we must simulate a large number of pairs, calculate
 362 the wave-function, and average Ψ^2 over all pairs in a given k^* bin. Essentially, we calculate Equation 8
 363 by hand:

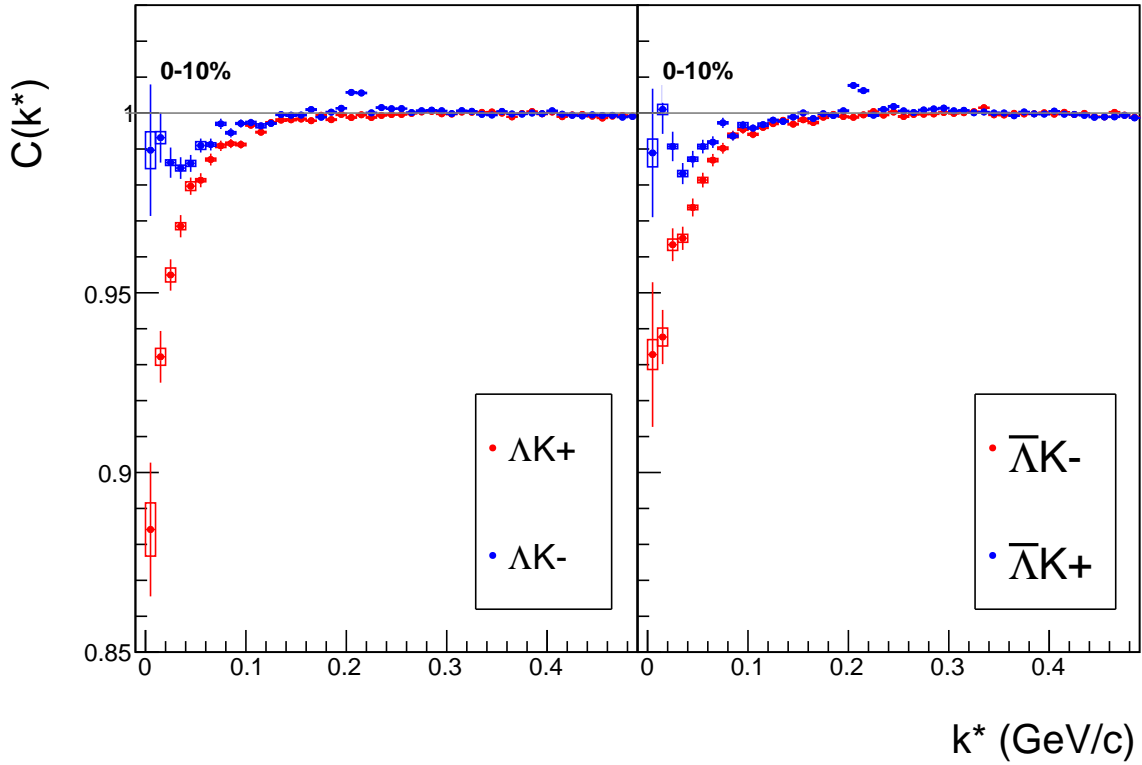


Fig. 14: Correlation Functions: ΛK^+ vs ΛK^- ($\bar{\Lambda} K^+$ vs $\bar{\Lambda} K^-$) for 0-10% centrality. The peak in $\Lambda K^- (\bar{\Lambda} K^+)$ at $k^* \approx 0.2$ GeV/c is due to the Ω^- resonance. The lines represent the statistical errors. (NOTE: This figure is slightly dated, and a new one will be generated which includes both statistical and systematic uncertainties)

$$\begin{aligned}
 C(\mathbf{k}^*) &= \sum_S \rho_S \int S(\mathbf{r}^*) |\Psi_{\mathbf{k}^*}^S(\mathbf{r}^*)|^2 d^3 \mathbf{r}^* \\
 &\longrightarrow C(|\mathbf{k}^*|) \equiv C(k^*) = \sum_S \rho_S \langle |\Psi^S(\mathbf{k}_i^*, \mathbf{r}_i^*)|^2 \rangle_i \\
 &\longrightarrow C(k^*) = \lambda \sum_S \rho_S \langle |\Psi^S(\mathbf{k}_i^*, \mathbf{r}_i^*)|^2 \rangle_i + (1 - \lambda)
 \end{aligned} \tag{12}$$

364 where $\langle \rangle_i$ represents an average over all pairs in a given k^* bin.

365 In summary, for a given k^* bin, we must draw $N_{pairs} \sim 10^4$ pairs, and for each pair:

366 1. Draw a random \mathbf{r}^* vector according to our Gaussian source distribution $S(\mathbf{r}^*)$

367 2. Draw a random \mathbf{k}^* vector satisfying the $|\mathbf{k}^*|$ restriction of the bin

368 – We draw from real k^* vectors obtained from the data

369 – However, we find that drawing from a distribution flat in k^* gives similar results

370 3. Construct the wave-function Ψ

371 After all pairs for a given k^* bin are simulated and wave-functions obtained, the results are averaged to
372 give the fit result.

373 Construction of the wave-functions, Equation 9, involves a number of complex functions not included
 374 in standard C++ or ROOT libraries (namely, $h(\eta)$, $\tilde{G}(\rho, \eta)$), and $F(-i\eta, 1, i\xi)$. These functions were
 375 even difficult to find and implement from elsewhere. Our solution was to embed a Mathematica kernel
 376 into our C++ code to evaluate these functions. However, having Mathematica work on-the-fly with the
 377 fitter was far too time consuming (fitter would have taken day, maybe weeks to finish). Our solution
 378 was to use Mathematica to create matrices representing these functions for different parameter values.
 379 During fitting, these matrices were then interpolated and the results used to build the wave-functions.
 380 This method decreased the running time dramatically, and we are not able to generate results in under \sim
 381 1 hour. This process will be explained in more detail in future versions of the note.

382 5.3 Momentum Resolution Corrections

383 Finite track momentum resolution causes the reconstructed momentum of a particle to smear around the
 384 true value. This, of course, also holds true for V0 particles. The effect is propagated up to the pairs
 385 of interest, which causes the reconstructed relative momentum (k_{Rec}^*) to differ from the true momentum
 386 (k_{True}^*). Smearing of the momentum typically will result in a suppression of the signal.

387 The effect of finite momentum resolution can be investigated using the MC data, for which both the true
 388 and reconstructed momenta are available. Figure 15 shows sample k_{True}^* vs. k_{Rec}^* plots for $\Lambda(\bar{\Lambda})K^\pm$ 0-
 389 10% analyses; Figure 15a was generated using same-event pairs, while Figure 15b was generated using
 390 mixed-event pairs (with $N_{mix} = 5$).

391 If there are no contaminations in our particle collection, the plots in Figure 15 should be smeared around
 392 $k_{True}^* = k_{Rec}^*$; this is mostly true in our analyses. However, there are some interesting features of our results
 393 which demonstrate a small (notice the log-scale on the z-axis) contamination in our particle collection.
 394 The structure around $k_{Rec}^* = k_{True}^* - 0.15$ is mainly caused by K_s^0 contamination in our $\Lambda(\bar{\Lambda})$ sample. The
 395 remaining structure not distributed about $k_{Rec}^* = k_{True}^*$ is due to π and e contamination in our K^\pm sample.
 396 These contaminations are more visible in Figure 16, which show k_{Rec}^* vs. k_{True}^* plots (for a small sample
 397 of the ΛK^+ 0-10% central analysis), for which the MC truth (i.e. true, known identity of the particle)
 398 was used to eliminate misidentified particles in the $K^+(a)$ and $\Lambda(b)$ collections. (NOTE: This is an old
 399 figure and is for a small sample of the data. A new version will be generated shortly. It, nonetheless,
 400 demonstrates the point well).

401 Information gained from looking at k_{Rec}^* vs k_{True}^* can be used to apply corrections to account for the
 402 effects of finite momentum resolution on the correlation functions. A typical method involves using the
 403 MC HIJING data to build two correlation functions, $C_{Rec}(k^*)$ and $C_{True}(k^*)$, using the generator-level
 404 momentum (k_{True}^*) and the measured detector-level momentum (k_{Rec}^*). The data is then corrected by
 405 multiplying by the ratio, C_{True}/C_{Rec} , before fitting. This essentially unsmears the data, which that can
 406 be compared directly to theoretical predictions and fits. Although this is conceptually simple, there are
 407 a couple of big disadvantages to this method. First, HIJING does not incorporate final-state interactions,
 408 so weights must be used when building same-event (numerator) distributions. These weights account for
 409 the interactions, and, in the absence of Coulomb interactions, can be calculated using Eq. 4. Of course,
 410 these weights are valid only for a particular set of fit parameters. Therefore, in the fitting process, during
 411 which the fitter explores a large parameter set, the corrections will not remain valid. As such, applying
 412 the momentum resolution correction and fitting becomes a long and drawn out iterative process. An initial
 413 parameter set is obtained (through fitting without momentum resolution corrections, theoretical models,
 414 or a good guess), then the MC data is run over to obtain the correction factor, the data is fit using the
 415 correction factor, a refined parameter set is extracted, the MC data is run over again to obtain the new
 416 correction factor, etc. This process continues until the parameter set stabilizes. The second issue concerns
 417 statistics. With the MC data available on the grid, we were not able to generate the statistics necessary
 418 to use the raw C_{True}/C_{Rec} ratio. The ratio was not stable, and when applied to the data, obscured the
 419 signal. Attempting to fit the ratio to use to generate the corrections also proved problematic. However, as

420 HIJING does not include final-state interactions, the same-event and mixed-event pairs are very similar
 421 (with the exception of things like energy and momentum conservation, etc). Therefore, one may build
 422 the numerator distribution using mixed-event pairs. This corresponds, more or less, to simply running a
 423 the weight generator through the detector framework.

424 A second approach is to use information gained from plots like those in Figure 15, which can be considered
 425 response matrices. The response matrix describes quantitatively how each k_{Rec}^* bin receives contributions
 426 from multiple k_{True}^* bins, and can be used to account for the effects of finite momentum resolution.
 427 With this approach, the resolution correction is applied on-the-fly during the fitting process by propagating
 428 the theoretical (fit) correlation function through the response matrix, according to:

$$C_{fit}(k_{Rec}^*) = \frac{\sum_{k_{True}^*} M_{k_{Rec}^*, k_{True}^*} C_{fit}(k_{True}^*)}{\sum_{k_{True}^*} M_{k_{Rec}^*, k_{True}^*}} \quad (13)$$

429 where $M_{k_{Rec}^*, k_{True}^*}$ is the response matrix (Figure 15), $C_{fit}(k_{True}^*)$ is the fit binned in k_{True}^* , and the denominator normalizes the result.

430 Equation 13 describes that, for a given k_{Rec}^* bin, the observed value of $C(k_{Rec}^*)$ is a weighted average of
 431 all $C(k_{True}^*)$ values, where the weights are the normalized number of counts in the $[k_{Rec}^*, k_{True}^*]$ bin. As
 432 seen in Figure 15, overwhelmingly the main contributions comes from the $k_{Rec}^* = k_{True}^*$ bins. Although
 433 the correction is small, it is non-negligible for the low- k^* region of the correlation function.

434 Here, the momentum resolution correction is applied to the fit, not the data. In other words, during
 435 fitting, the theoretical correlation function is smeared just as real data would be, instead of unsmearing
 436 the data. This may not be ideal for the theorist attempting to compare a model to experimental data, but
 437 it leaves the experimental data unadulterated. The current analyses use this second approach to applying
 438 momentum resolution corrections because of two major advantages. First, the MC data must be analyzed
 439 only once, and no assumptions about the fit are needed. Secondly, the momentum resolution correction
 440 is applied on-the-fly by the fitter, delegating the iterative process to a computer instead of the user.

442 5.4 Residual Correlations

443 The purpose of this analysis is study the interaction and scale of the emitting source of the pairs. In order
 444 to obtain correct results, it is important for our particle collections to consist of primary particles. In
 445 practice, this is difficult to achieve for our Λ and $\bar{\Lambda}$ collections. Many of our Λ particles are not primary,
 446 but originate as decay products from other hyperons, including Σ^0 , Ξ^- , Ξ^0 and Ω^- . In these decays,
 447 the Λ carries away a momentum very similar to that of its parent. As a result, the correlation function
 448 between a secondary Λ and, for instance, a K^+ will be sensitive to, and dependent upon, the interaction
 449 between the parent of the Λ and the K^+ . In effect, the correlation between the parent of the Λ and the K^+
 450 (ex. $\Sigma^0 K^+$) will be visible, although smeared out, in the ΛK^+ data. We call this a residual correlation
 451 resulting from feed-down.

452 As it is difficult for us to eliminate these residual correlations in our analyses, we must attempt to account
 453 for them in our fitter. To achieve this, we will simultaneously fit the data for both the primary correlation
 454 function and the residual correlations. For example, in the simple case of a ΛK^+ analysis with residuals
 455 arising solely from $\Sigma^0 K^+$ feed-down:

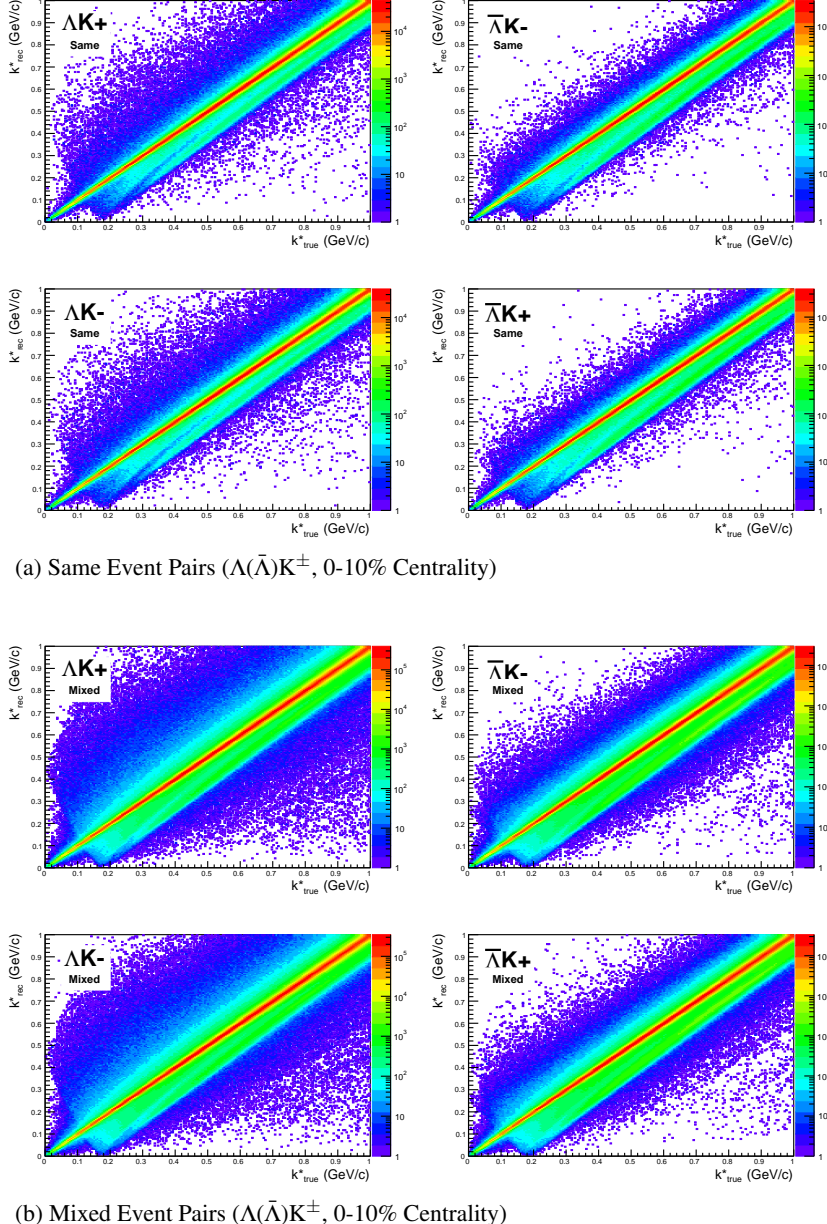
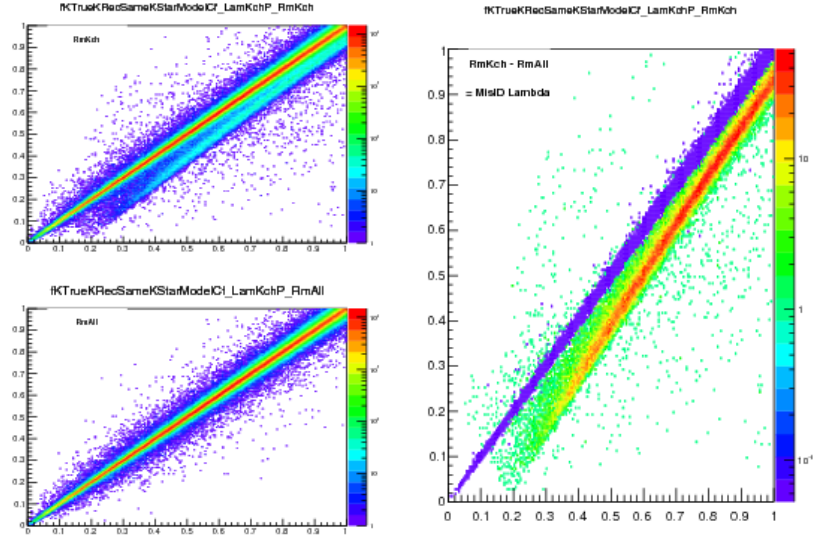


Fig. 15: Sample k_{True}^* vs. k_{Rec}^* plot for $\Lambda(\bar{\Lambda})K^\pm$ 0-10% analyses. The structure which appears around $k_{Rec}^* = k_{True}^* - 0.15$ is mainly caused by K_S^0 contamination in our $\Lambda(\bar{\Lambda})$ sample. The remaining structure not distributed about $k_{Rec}^* = k_{True}^*$ is due to π and e contamination in our K^\pm sample. These contaminations are more clearly visible in Figure 16

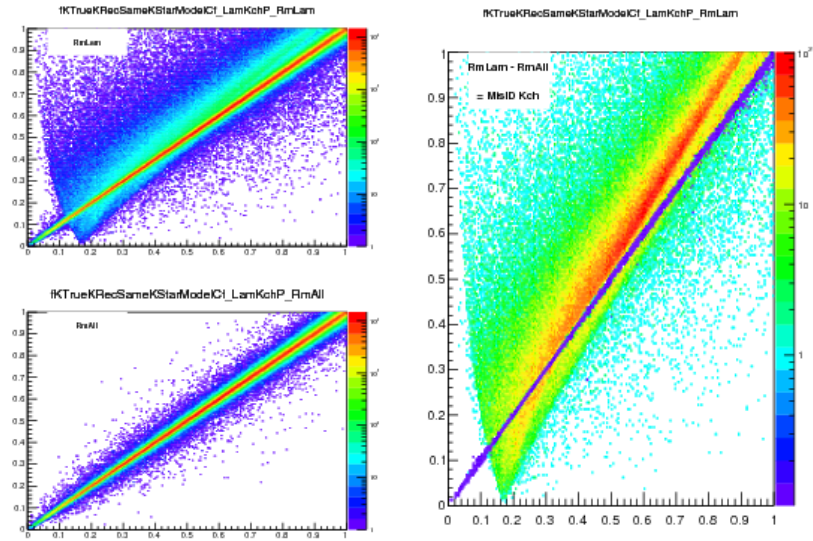
$$C_{measured}(k_{\Lambda K^+}^*) = 1 + \lambda_{\Lambda K^+}[C_{\Lambda K^+}(k_{\Lambda K^+}^*) - 1] + \lambda_{\Sigma^0 K^+}[C_{\Sigma^0 K^+}(k_{\Lambda K^+}^*) - 1]$$

$$C_{\Sigma^0 K^+}(k_{\Lambda K^+}^*) \equiv \sum_{k_{\Sigma^0 K^+}^*} \frac{C_{\Sigma^0 K^+}(k_{\Sigma^0 K^+}^*) T(k_{\Sigma^0 K^+}^*, k_{\Lambda K^+}^*)}{T(k_{\Sigma^0 K^+}^*, k_{\Lambda K^+}^*)} \quad (14)$$

456 $C_{\Sigma^0 K^+}(k_{\Sigma^0 K^+}^*)$ is the $\Sigma^0 K^+$ correlation function from, for instance, Equation 4, and T is the transform
 457 matrix generated with THERMINATOR. This equation can be easily extended to include feed-down
 458 from more sourced:



(a) (Top Left) All misidentified K^+ excluded. (Bottom Left) All misidentified Λ and K^+ excluded. (Right) The difference of (Top Left) - (Bottom Left), which reveals the contamination in our Λ collection. The structure which appears around $k*_{Rec} = k*_{True} - 0.15$ is mainly caused by K_S^0 contamination in our $\Lambda(\bar{\Lambda})$ sample.



(b) (Top Left) All misidentified Λ excluded. (Bottom Left) All misidentified Λ and K^+ excluded. (Right) The difference of (Top Left) - (Bottom Left), which reveals the contamination in our K^+ collection. The structure not distributed about $k*_{Rec} = k*_{True}$ is due to π and e^- contamination in our K^\pm sample.

Fig. 16: Note: This is an old figure and is for a small sample of the data. A new version will be generated shortly.
 $y\text{-axis} = k*_{Rec}$, $x\text{-axis} = k*_{True}$.

(Left) $k*_{Rec}$ vs. $k*_{True}$ plots for a small sample of the ΛK^+ 0-10% central analysis, MC truth was used to eliminate misidentified particles in the K^+ (a) and Λ (b) collections. (Right) The difference of the top left and bottom left plots. Contaminations in our particle collections are clearly visible. Figure (a) demonstrates a K_S^0 contamination in our Λ collection; Figure (b) demonstrates a π and e^- contamination in our K^\pm collection.

$$C_{measured}(k*_{\Lambda K}) = \sum_i \lambda_i C_i(k*_{\Lambda K}) \quad (15)$$

- 459 The framework for extracting the necessary transform matrices from the THERMINATOR data is already
 460 in place, and has been used to generate the examples from ΛK^+ and $\bar{\Lambda} K^+$ analyses shown in Figures 17
 461 and 18. However, these residual correlations have not yet been implemented in the fitter.
 462 There is an obvious added complication here, as, for instance, the $\Xi^- K^\pm$ residuals necessitate the in-
 463 clusion of the CoulombFitter into the process. The complication of combining the two fitters is not as
 464 troubling as the increase in fitting time that this is sure to bring. Additionally, in the future, we may
 465 combine our ΛK and ΞK analyses to be fit simultaneously.

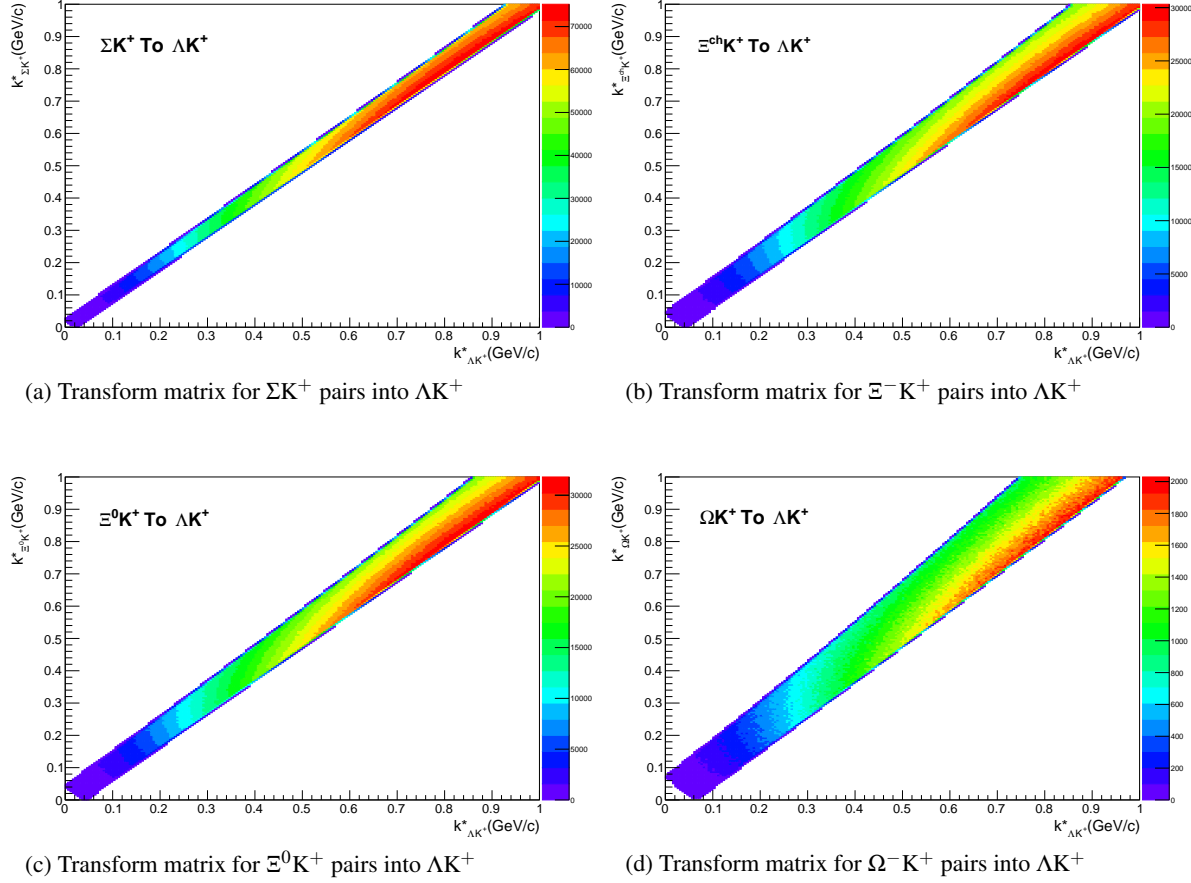


Fig. 17: Transform Matrices generated with THERMINATOR for ΛK^+ Analysis

466 6 Systematic Errors

- 467 In order to understand my systematic uncertainties, the analysis code was run many times using slightly
 468 different values for a number of important cuts, and the results were compared.
 469 In order to quantify the systematic errors on the data, all correlation functions built using all varied cut
 470 values were bin-by-bin averaged, and the resulting variance of each bin was taken as the systematic error.
 471 The cuts which were utilized in this study are presented in Sections 6.1.1 (ΛK_S^0) and 6.2.1 (ΛK^\pm).
 472 Similarly, the fit parameters extracted from all of these correlation functions were averaged, and the
 473 resulting variances were taken as the systematic errors for the fit parameters. As with the systematic
 474 errors on the data, this was performed for all varied cut values. Additionally, a systematic analysis was
 475 done on our fit method (which, for now, just includes our choice of fit range). These two sources of
 476 uncertainty were combined in quadrature to obtain the final systematic uncertainties on the extracted fit
 477 parameters.

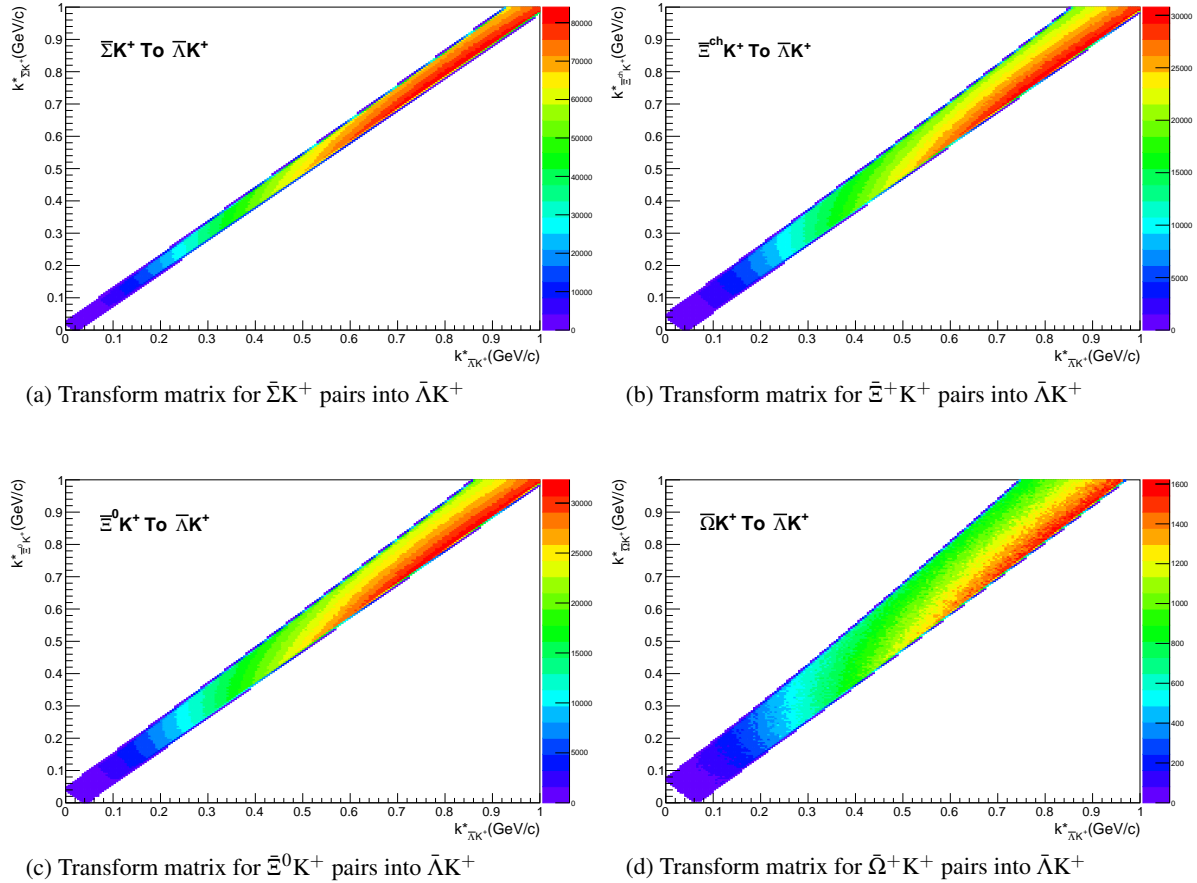


Fig. 18: Transform Matrices generated with THERMINATOR for $\bar{\Lambda}K^+$ Analysis

478 6.1 Systematic Errors: ΛK_S^0

479 6.1.1 Particle and Pair Cuts

480 The cuts included in the systematic study, as well as the values used in the variations, are listed below.
 481 Note, the central value corresponds to that used in the analysis.

- 482 1. DCA $\Lambda(\bar{\Lambda})$: {4, 5, 6 mm}
- 483 2. DCA K_S^0 : {2, 3, 4 mm}
- 484 3. DCA $\Lambda(\bar{\Lambda})$ Daughters: {3, 4, 5 mm}
- 485 4. DCA K_S^0 Daughters: {2, 3, 4 mm}
- 486 5. $\Lambda(\bar{\Lambda})$ Cosine of Pointing Angle: {0.9992, 0.9993, 0.9994}
- 487 6. K_S^0 Cosine of Pointing Angle: {0.9992, 0.9993, 0.9994}
- 488 7. DCA to Primary Vertex of $p(\bar{p})$ Daughter of $\Lambda(\bar{\Lambda})$: {0.5, 1, 2 mm}
- 489 8. DCA to Primary Vertex of $\pi^-(\pi^+)$ Daughter of $\Lambda(\bar{\Lambda})$: {2, 3, 4 mm}
- 490 9. DCA to Primary Vertex of π^+ Daughter of K_S^0 : {2, 3, 4 mm}
- 491 10. DCA to Primary Vertex of π^- Daughter of K_S^0 : {2, 3, 4 mm}
- 492 11. Average Separation of Like-Charge Daughters: {5, 6, 7 cm}

493 6.1.2 Non-Flat Background

494 Still needs to be done. Currently, we fit our non-flat background with a linear function. We will also use
495 a quadratic form, and analyze how this choice affects our extracted parameter sets.

496 6.1.3 Fit Range

497 Our choice of k^* fit range was varied by $\pm 25\%$. The resulting uncertainties in the extracted parameter
498 sets were combined with our uncertainties arising from our particle and pair cuts.

499 6.2 Systematic Errors: ΛK^\pm
500 6.2.1 Particle and Pair Cuts

501 The cuts included in the systematic study, as well as the values used in the variations, are listed below.
502 Note, the central value corresponds to that used in the analysis.

- 503 1. DCA $\Lambda(\bar{\Lambda})$: {4, 5, 6 mm}
- 504 2. DCA $\Lambda(\bar{\Lambda})$ Daughters: {3, 4, 5 mm}
- 505 3. $\Lambda(\bar{\Lambda})$ Cosine of Pointing Angle: {0.9992, 0.9993, 0.9994}
- 506 4. DCA to Primary Vertex of $p(\bar{p})$ Daughter of $\Lambda(\bar{\Lambda})$: {0.5, 1, 2 mm}
- 507 5. DCA to Primary Vertex of $\pi^-(\pi^+)$ Daughter of $\Lambda(\bar{\Lambda})$: {2, 3, 4 mm}
- 508 6. Average Separation of $\Lambda(\bar{\Lambda})$ Daughter with Same Charge as K^\pm : {7, 8, 9 cm}

509 6.2.2 Non-Flat Background

510 Still needs to be done. Currently, we fit our non-flat background with a linear function. We will also use
511 a quadratic form, and analyze how this choice affects our extracted parameter sets.

512 6.2.3 Fit Range

513 Our choice of k^* fit range was varied by $\pm 25\%$. The resulting uncertainties in the extracted parameter
514 sets were combined with our uncertainties arising from our particle and pair cuts.

515 6.3 Systematic Errors: ΞK^\pm
516 6.3.1 Particle and Pair Cuts

517 The cuts included in the systematic study, as well as the values used in the variations, are listed below.
518 Note, the central value corresponds to that used in the analysis.

- 519 1. Max. DCA $\Xi(\bar{\Xi})$: {x, y, z mm}
- 520 2. Max. DCA $\Xi(\bar{\Xi})$ Daughters: {x, y, z mm}
- 521 3. Min. $\Xi(\bar{\Xi})$ Cosine of Pointing Angle to Primary Vertex: {0.9991, 0.9992, 0.9993}
- 522 4. Min. $\Lambda(\bar{\Lambda})$ Cosine of Pointing Angle to $\Xi(\bar{\Xi})$ Decay Vertex: {0.9992, 0.9993, 0.9994}
- 523 5. Min. DCA Bachelor π : {0.2, 0.3, 0.4 mm}
- 524 6. Min. DCA $\Lambda(\bar{\Lambda})$: {0.5, 1, 2 mm}

- 525 7. Max. DCA $\Lambda(\bar{\Lambda})$ Daughters: {3, 4, 5 mm}
- 526 8. Min. $\Lambda(\bar{\Lambda})$ Cosine of Pointing Angle To Primary Vertex: {0.9992, 0.9993, 0.9994}
- 527 9. Min. DCA to Primary Vertex of $p(\bar{p})$ Daughter of $\Lambda(\bar{\Lambda})$: {0.5, 1, 2 mm}
- 528 10. Min. DCA to Primary Vertex of $\pi^-(\pi^+)$ Daughter of $\Lambda(\bar{\Lambda})$: {2, 3, 4 mm}
- 529 11. Min. Average Separation of $\Lambda(\bar{\Lambda})$ Daughter and K^\pm with like charge: {7, 8, 9 cm}
- 530 12. Min. Average Separation of Bachelor π and K^\pm with like charge: {x, y, z cm}
- 531 13. Max. DCA to Primary Vertex in Transverse Plane of K^\pm : {1.92, 2.4, 2.88}
- 532 14. Max. DCA to Primary Vertex in Longitudinal Direction of K^\pm : {2.4, 3.0, 3.6}

533 **6.3.2 Non-Flat Background**

534 Still needs to be done. Currently, we fit our non-flat background with a linear function. We will also use
 535 a quadratic form, and analyze how this choice affects our extracted parameter sets.

536 **6.3.3 Fit Range**

537 Our choice of k^* fit range was varied by $\pm 25\%$. The resulting uncertainties in the extracted parameter
 538 sets were combined with our uncertainties arising from our particle and pair cuts.

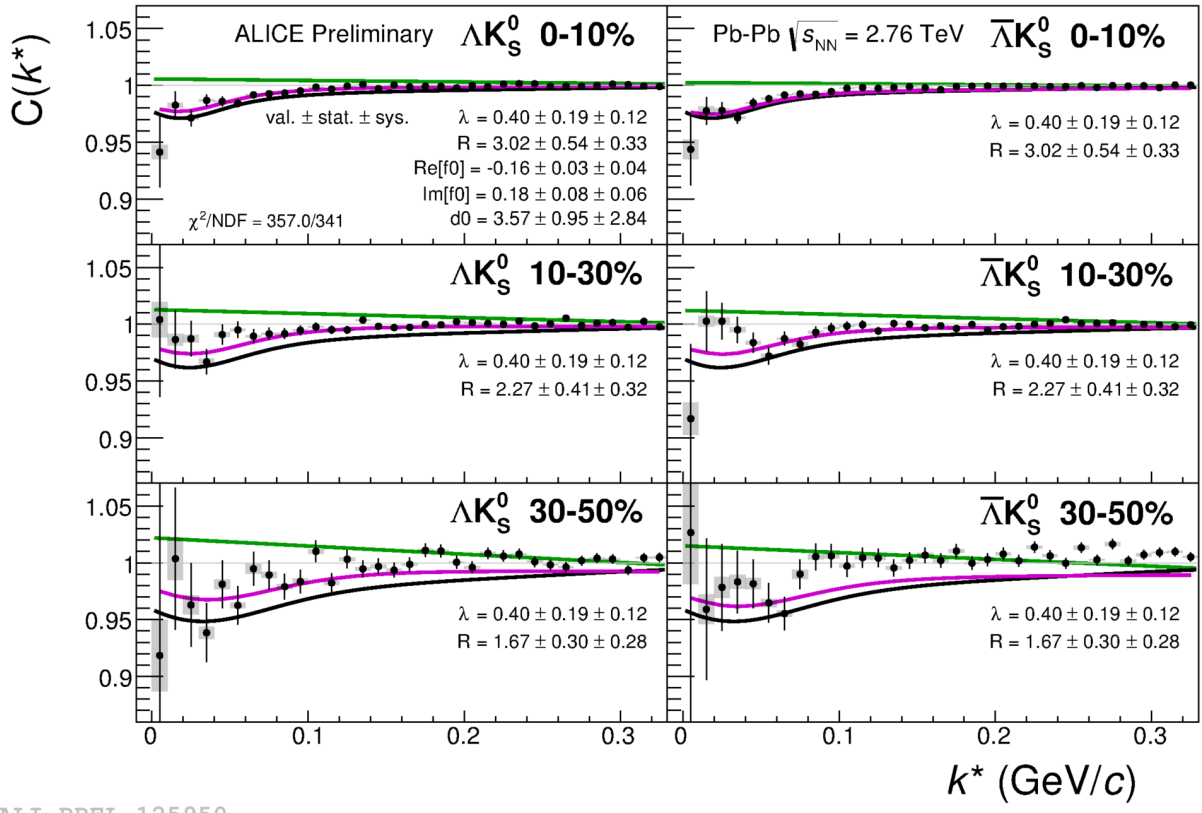
539 **7 Results and Discussion**

540 **7.1 Results: ΛK_S^0 and ΛK^\pm**

541 Figures 19, 21, and 23 (Section 7) show experimental data with fits for all studied centralities for ΛK_S^0
 542 with $\bar{\Lambda} K_S^0$, ΛK^+ with $\bar{\Lambda} K^-$, and ΛK^- with $\bar{\Lambda} K^+$, respectively. The parameter sets extracted from the fits
 543 can be found in Tables 1 and 2. All correlation functions were normalized in the range $0.32 < k^* < 0.40$
 544 GeV/c, and fit in the range $0.0 < k^* < 0.30$ GeV/c. For the ΛK^- and $\bar{\Lambda} K^+$ analyses, the region $0.19 < k^* < 0.23$ GeV/c was excluded from the fit to exclude the bump caused by the Ω^- resonance. The
 546 non-flat background was fit with a linear form from $0.6 < k^* < 0.9$ GeV/c. The theoretical fit function
 547 was then multiplied by this background during the fitting process.

548 In the figures (19, 21, and 23), the black solid line represents the “raw” fit, i.e. not corrected for momentum
 549 resolution effects nor non-flat background. The green line shows the fit to the non-flat background.
 550 The purple points show the fit after momentum resolution and non-flat background corrections have been
 551 applied. The initial values of the parameters is listed, as well as the final fit values with uncertainties.

552 For the ΛK_S^0 fits, R was restricted to [2.0, 10.0 fm] and Λ was restricted to [0.1, 0.8]. This gave the lowest
 553 χ^2 value, but loosening this restriction changes the fit parameters slightly. Notice, the 10-30% radius is
 554 at its limit, as is λ from the 30-50% ΛK_S^0 analysis. This accounts for the 0.000 systematic uncertainty of
 555 the 10-30% R value currently quoted in Table 1. An estimate for this uncertainty should be included in
 556 the next version of this note. In the future, we may need to throw out the 30-50% data from the fit, but
 557 this is not ideal.



ALI-PREL-125950

Fig. 19: Fits to the ΛK_S^0 (left) and $\bar{\Lambda} K_S^0$ (right) data for the centralities 0-10% (top), 10-30% (middle), and 30-50% (bottom). The lines represent the statistical errors, while the boxes represent the systematic errors. Each has unique λ and normalization parameters. The radii are shared amongst like centralities; the scattering parameters ($\text{Re}[f_0]$, $\text{Im}[f_0]$, d_0) are shared amongst all. The black solid line represents the “raw” fit, i.e. not corrected for momentum resolution effects nor non-flat background. The green line shows the fit to the non-flat background. The purple points show the fit after momentum resolution and non-flat background corrections have been applied. The initial values of the parameters is listed, as well as the final fit values with uncertainties. Here, R was restricted to [2.,10.] and Λ was restricted to [0.1,0.8].

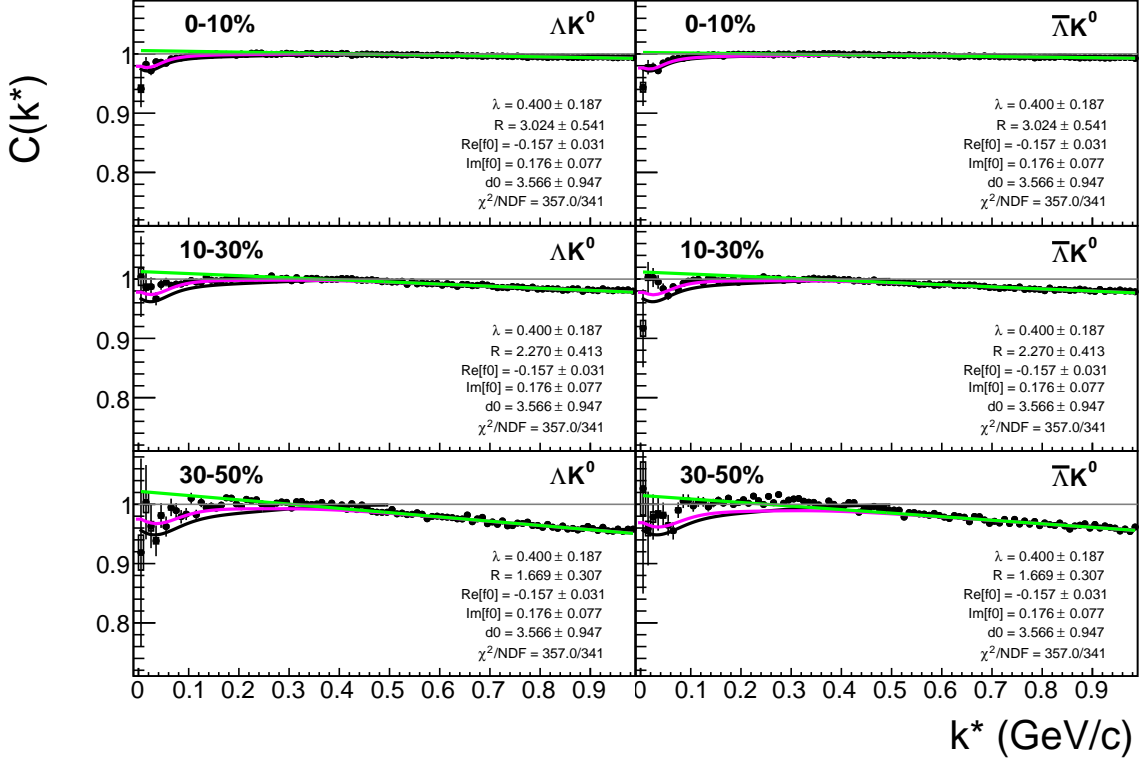
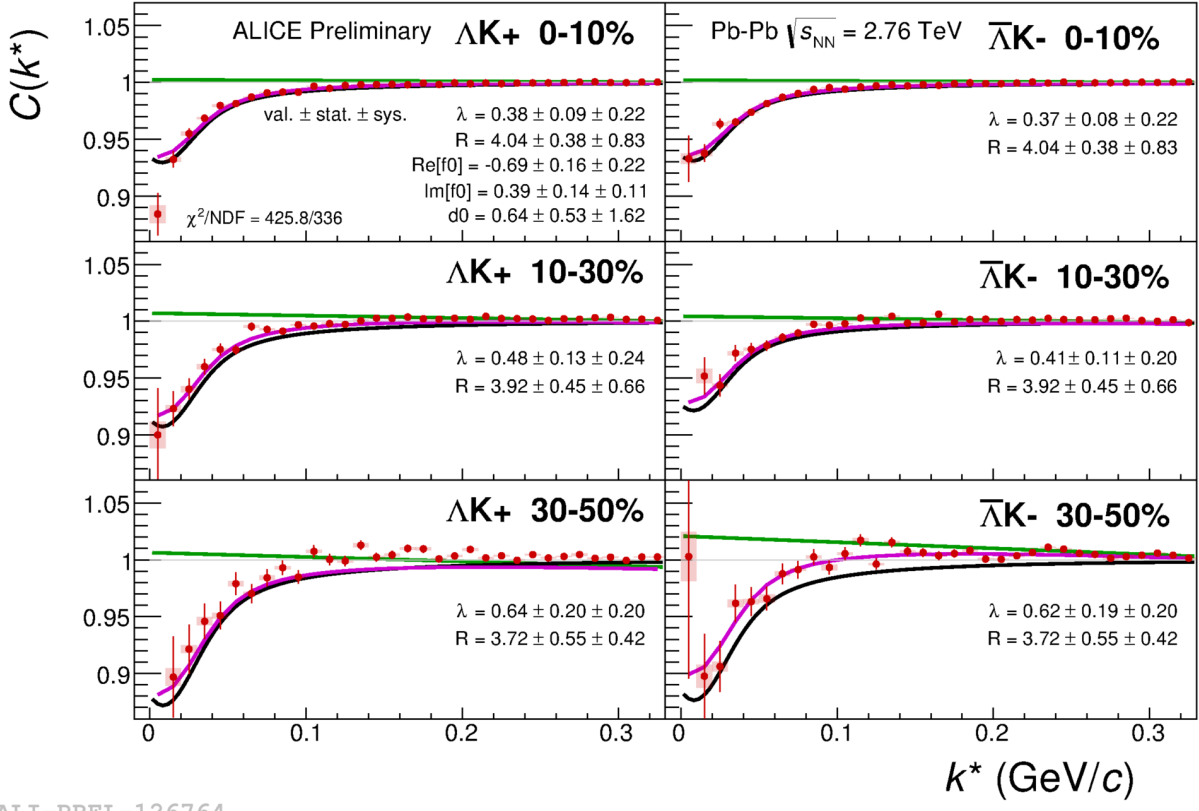


Fig. 20: Same as Fig. 19, but with a wider range of view. Fits to the ΛK_S^0 (left) and $\bar{\Lambda} K_S^0$ (right) data for the centralities 0-10% (top), 10-30% (middle), and 30-50% (bottom). The lines represent the statistical errors, while the boxes represent the systematic errors. Each has unique λ and normalization parameters. The radii are shared amongst like centralities; the scattering parameters ($\mathbb{R} f_0$, $\mathbb{I} f_0$, d_0) are shared amongst all. The black solid line represents the “raw” fit, i.e. not corrected for momentum resolution effects nor non-flat background. The green line shows the fit to the non-flat background. The purple points show the fit after momentum resolution and non-flat background corrections have been applied. The initial values of the parameters is listed, as well as the final fit values with uncertainties. Here, R was restricted to [2.,10.] and Λ was restricted to [0.1,0.8].



ALI-PREL-126764

Fig. 21: Fits to the ΛK^+ (left) and $\bar{\Lambda} K^-$ (right) data for the centralities 0-10% (top), 10-30% (middle), and 30-50% (bottom). The lines represent the statistical errors, while the boxes represent the systematic errors. Each has unique λ and normalization parameters. The radii are shared amongst like centralities; the scattering parameters ($Re[f_0]$, $Im[f_0]$, d_0) are shared amongst all. The black solid line represents the “raw” fit, i.e. not corrected for momentum resolution effects nor non-flat background. The green line shows the fit to the non-flat background. The purple points show the fit after momentum resolution and non-flat background corrections have been applied. The initial values of the parameters is listed, as well as the final fit values with uncertainties.

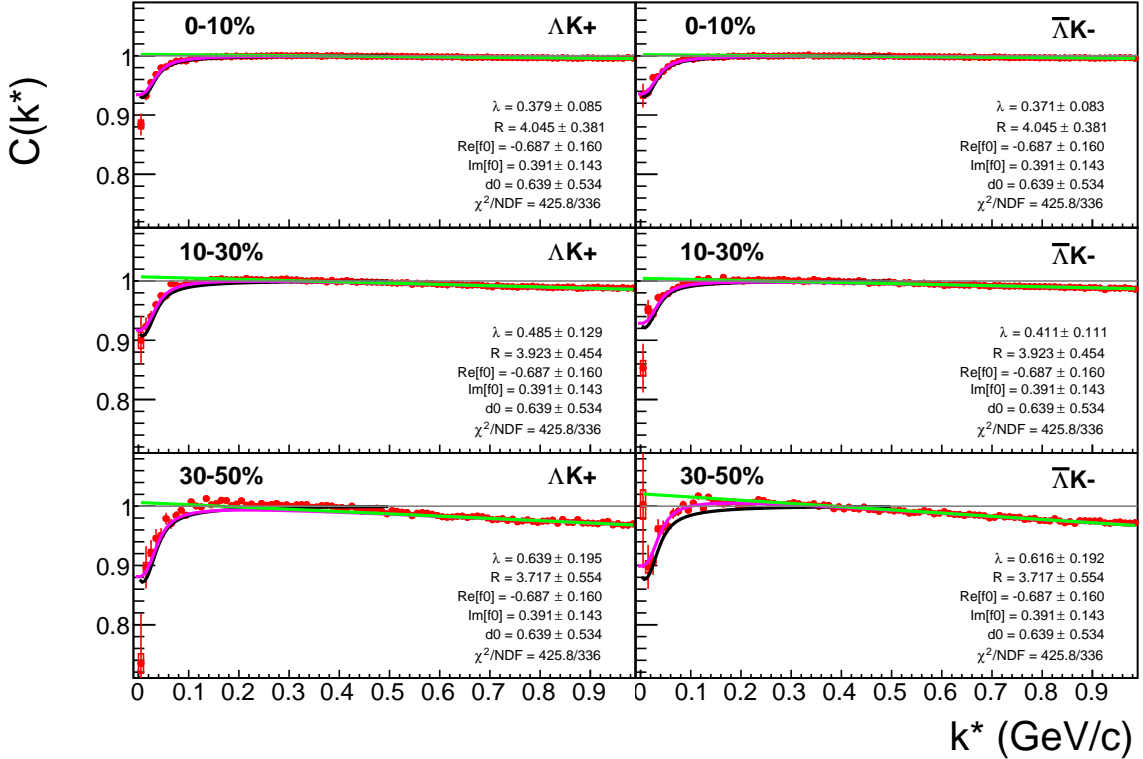


Fig. 22: Same as Fig. 21, but with a wider range of view. Fits to the ΛK^+ (left) and $\bar{\Lambda} K^-$ (right) data for the centralities 0-10% (top), 10-30% (middle), and 30-50% (bottom). The lines represent the statistical errors, while the boxes represent the systematic errors. Each has unique λ and normalization parameters. The radii are shared amongst like centralities; the scattering parameters ($\mathbb{R} f_0$, $\mathbb{I} f_0$, d_0) are shared amongst all. The black solid line represents the “raw” fit, i.e. not corrected for momentum resolution effects nor non-flat background. The green line shows the fit to the non-flat background. The purple points show the fit after momentum resolution and non-flat background corrections have been applied. The initial values of the parameters is listed, as well as the final fit values with uncertainties.

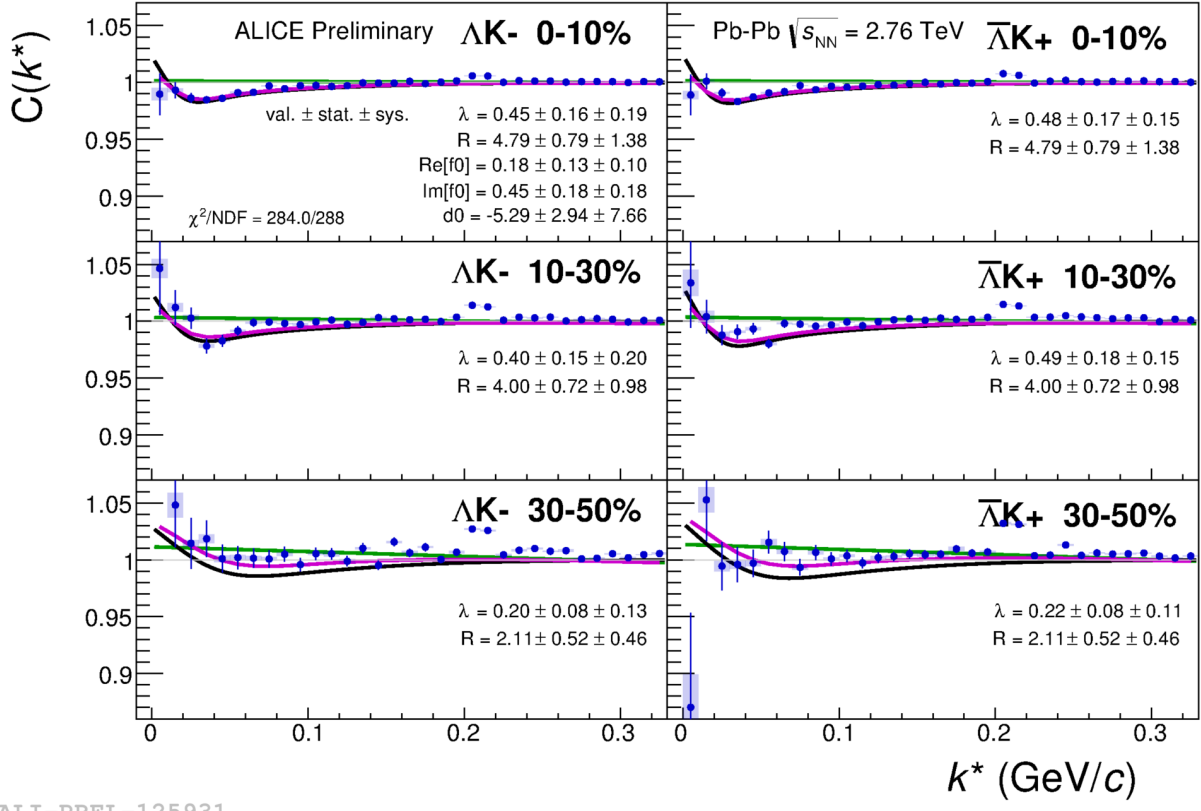


Fig. 23: Fits to the ΛK^- (left) with $\bar{\Lambda} K^+$ (right) data for the centralities 0-10% (top), 10-30% (middle), and 30-50% (bottom). The lines represent the statistical errors, while the boxes represent the systematic errors. Each has unique λ and normalization parameters. The radii are shared amongst like centralities; the scattering parameters ($\text{Re}[f_0]$, $\text{Im}[f_0]$, d_0) are shared amongst all. The black solid line represents the “raw” fit, i.e. not corrected for momentum resolution effects nor non-flat background. The green line shows the fit to the non-flat background. The purple points show the fit after momentum resolution and non-flat background corrections have been applied. The initial values of the parameters is listed, as well as the final fit values with uncertainties.

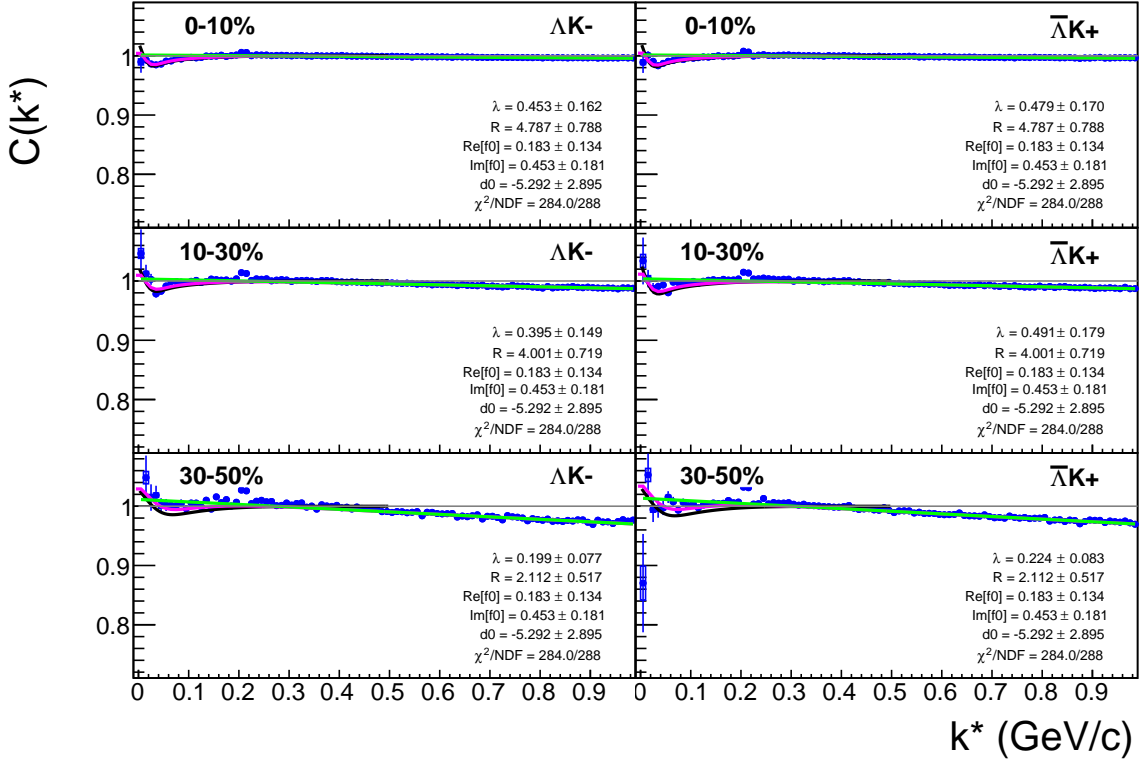


Fig. 24: Same as Fig. 23, but with a wider range of view. Fits to the ΛK^- (left) with $\bar{\Lambda} K^+$ (right) data for the centralities 0-10% (top), 10-30% (middle), and 30-50% (bottom). The lines represent the statistical errors, while the boxes represent the systematic errors. Each has unique λ and normalization parameters. The radii are shared amongst like centralities; the scattering parameters ($\mathbb{R}f_0$, $\mathbb{I}f_0$, d_0) are shared amongst all. The black solid line represents the “raw” fit, i.e. not corrected for momentum resolution effects nor non-flat background. The green line shows the fit to the non-flat background. The purple points show the fit after momentum resolution and non-flat background corrections have been applied. The initial values of the parameters is listed, as well as the final fit values with uncertainties.

Fit Results $\Lambda(\bar{\Lambda})K_S^0$						
Pair Type	Centrality	Fit Parameters				
		λ	R	$\mathbb{R}f_0$	$\mathbb{I}f_0$	d_0
ΛK_S^0	0-10%	0.400 ± 0.187 (stat.) ± 0.116 (sys.)	3.024 ± 0.541 (stat.) ± 0.329 (sys.)	-0.157 ± 0.031 (stat.) ± 0.043 (sys.)	0.176 ± 0.077 (stat.) ± 0.059 (sys.)	3.566 ± 0.947 (stat.) ± 2.836 (sys.)
	10-30%		2.270 ± 0.413 (stat.) ± 0.324 (sys.)			
	30-50%		1.669 ± 0.307 (stat.) ± 0.280 (sys.)			
$\bar{\Lambda} K_S^0$	0-10%	0.400 ± 0.187 (stat.) ± 0.116 (sys.)	3.024 ± 0.541 (stat.) ± 0.329 (sys.)	-0.157 ± 0.031 (stat.) ± 0.043 (sys.)	0.176 ± 0.077 (stat.) ± 0.059 (sys.)	3.566 ± 0.947 (stat.) ± 2.836 (sys.)
	10-30%		2.270 ± 0.413 (stat.) ± 0.324 (sys.)			
	30-50%		1.669 ± 0.307 (stat.) ± 0.280 (sys.)			

Table 1: Fit Results $\Lambda(\bar{\Lambda})K_S^0$. Each pair is fit simultaneously with its conjugate (ie. ΛK_S^0 with $\bar{\Lambda} K_S^0$) across all centralities (0-10%, 10-30%, 30-50%), for a total of 6 simultaneous analyses in the fit. Each analysis has a unique λ and normalization parameter. The radii are shared between analyses of like centrality, as these should have similar source sizes. The scattering parameters ($\mathbb{R}f_0$, $\mathbb{I}f_0$, d_0) are shared amongst all. The fit is done on the data with only statistical error bars. The errors marked as “stat.” are those returned by MINUIT. The errors marked as “sys.” are those which result from my systematic analysis (as outlined in Section 6).

Fit Results $\Lambda(\bar{\Lambda})K^\pm$						
Pair Type	Centrality	Fit Parameters				
		λ	R	$\mathbb{R}f_0$	$\mathbb{I}f_0$	d_0
ΛK^+	0-10%	0.379 ± 0.085 (stat.) ± 0.220 (sys.)	4.045 ± 0.381 (stat.) ± 0.830 (sys.)	-0.687 ± 0.160 (stat.) ± 0.223 (sys.)	0.391 ± 0.143 (stat.) ± 0.111 (sys.)	0.639 ± 0.534 (stat.) ± 1.621 (sys.)
	10-30%	0.485 ± 0.129 (stat.) ± 0.241 (sys.)	3.923 ± 0.454 (stat.) ± 0.663 (sys.)			
	30-50%	0.639 ± 0.195 (stat.) ± 0.204 (sys.)	3.717 ± 0.554 (stat.) ± 0.420 (sys.)			
$\bar{\Lambda} K^-$	0-10%	0.371 ± 0.083 (stat.) ± 0.217 (sys.)	4.045 ± 0.381 (stat.) ± 0.830 (sys.)	0.183 ± 0.134 (stat.) ± 0.095 (sys.)	0.453 ± 0.181 (stat.) ± 0.184 (sys.)	-5.292 ± 2.895 (stat.) ± 7.658 (sys.)
	10-30%	0.411 ± 0.111 (stat.) ± 0.201 (sys.)	3.923 ± 0.454 (stat.) ± 0.663 (sys.)			
	30-50%	0.616 ± 0.192 (stat.) ± 0.203 (sys.)	3.717 ± 0.554 (stat.) ± 0.420 (sys.)			
ΛK^-	0-10%	0.453 ± 0.162 (stat.) ± 0.186 (sys.)	4.787 ± 0.788 (stat.) ± 1.375 (sys.)	0.183 ± 0.134 (stat.) ± 0.095 (sys.)	0.453 ± 0.181 (stat.) ± 0.184 (sys.)	-5.292 ± 2.895 (stat.) ± 7.658 (sys.)
	10-30%	0.395 ± 0.149 (stat.) ± 0.198 (sys.)	4.001 ± 0.719 (stat.) ± 0.978 (sys.)			
	30-50%	0.199 ± 0.077 (stat.) ± 0.132 (sys.)	2.112 ± 0.517 (stat.) ± 0.457 (sys.)			
$\bar{\Lambda} K^+$	0-10%	0.479 ± 0.170 (stat.) ± 0.152 (sys.)	4.787 ± 0.788 (stat.) ± 1.375 (sys.)	0.183 ± 0.134 (stat.) ± 0.095 (sys.)	0.453 ± 0.181 (stat.) ± 0.184 (sys.)	-5.292 ± 2.895 (stat.) ± 7.658 (sys.)
	10-30%	0.491 ± 0.179 (stat.) ± 0.148 (sys.)	4.001 ± 0.719 (stat.) ± 0.978 (sys.)			
	30-50%	0.224 ± 0.083 (stat.) ± 0.106 (sys.)	2.112 ± 0.517 (stat.) ± 0.457 (sys.)			

Table 2: Fit Results $\Lambda(\bar{\Lambda})K^\pm$ Each pair is fit simultaneously with its conjugate (ie. ΛK^+ with $\bar{\Lambda} K^-$ and ΛK^- with $\bar{\Lambda} K^+$) across all centralities (0-10%, 10-30%, 30-50%), for a total of 6 simultaneous analyses in the fit. Each analysis has a unique λ and normalization parameter. The radii are shared between analyses of like centrality, as these should have similar source sizes. The scattering parameters ($\mathbb{R}f_0$, $\mathbb{I}f_0$, d_0) are shared amongst all. The fit is done on the data with only statistical error bars. The errors marked as “stat.” are those returned by MINUIT. The errors marked as “sys.” are those which result from my systematic analysis (as outlined in Section 6).

Fit Parameters (value \pm statistical error \pm systematic error)

Pair Type	Centrality	R		
		$\Re f_0$	$\Im f_0$	d_0
$\Lambda K^+ & \bar{\Lambda} K^-$	0-10%		$4.04 \pm 0.38 \pm 0.83$	
	10-30%		$3.92 \pm 0.45 \pm 0.66$	
	30-50%		$3.72 \pm 0.55 \pm 0.42$	
		$-0.69 \pm 0.16 \pm 0.22$	$0.39 \pm 0.14 \pm 0.11$	$0.64 \pm 0.53 \pm 1.62$
$\Lambda K^- & \bar{\Lambda} K^+$	0-10%		$4.79 \pm 0.79 \pm 1.38$	
	10-30%		$4.00 \pm 0.72 \pm 0.98$	
	30-50%		$2.11 \pm 0.52 \pm 0.46$	
		$0.18 \pm 0.13 \pm 0.10$	$0.45 \pm 0.18 \pm 0.18$	$-5.29 \pm 2.94 \pm 7.66$
$\Lambda K_S^0 & \bar{\Lambda} K_S^0$	0-10%		$3.02 \pm 0.54 \pm 0.33$	
	10-30%		$2.27 \pm 0.41 \pm 0.32$	
	30-50%		$1.67 \pm 0.30 \pm 0.28$	
		$-0.16 \pm 0.03 \pm 0.04$	$0.18 \pm 0.08 \pm 0.06$	$3.57 \pm 0.95 \pm 2.84$

558 **7.2 Results: ΞK^\pm**

559 Even without any fits to the data, the fact that the $\Xi^- K^+$ data dips below unity is exciting, as this cannot
 560 occur purely from a Coulomb interaction. We hope that this dip signifies that we are able to peer through
 561 the overwhelming contribution from the Coulomb interaction to see the effects arising from the strong
 562 interaction.

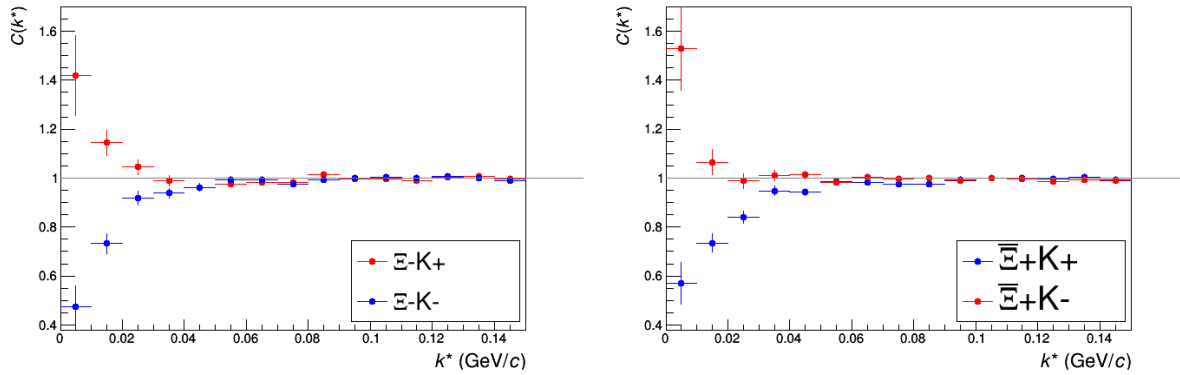


Fig. 25: ΞK^\pm Results for 0-10% Centrality

563 **8 To Do**

References

- [1] R. Lednicky and V. L. Lyuboshitz. *Sov. J. Nucl. Phys.*, 35:770, 1982.
- [2] Michael Annan Lisa, Scott Pratt, Ron Soltz, and Urs Wiedemann. Femtoscopy in relativistic heavy ion collisions. *Ann. Rev. Nucl. Part. Sci.*, 55:357–402, 2005.
- [3] Richard Lednicky. Finite-size effects on two-particle production in continuous and discrete spectrum. *Phys. Part. Nucl.*, 40:307–352, 2009.

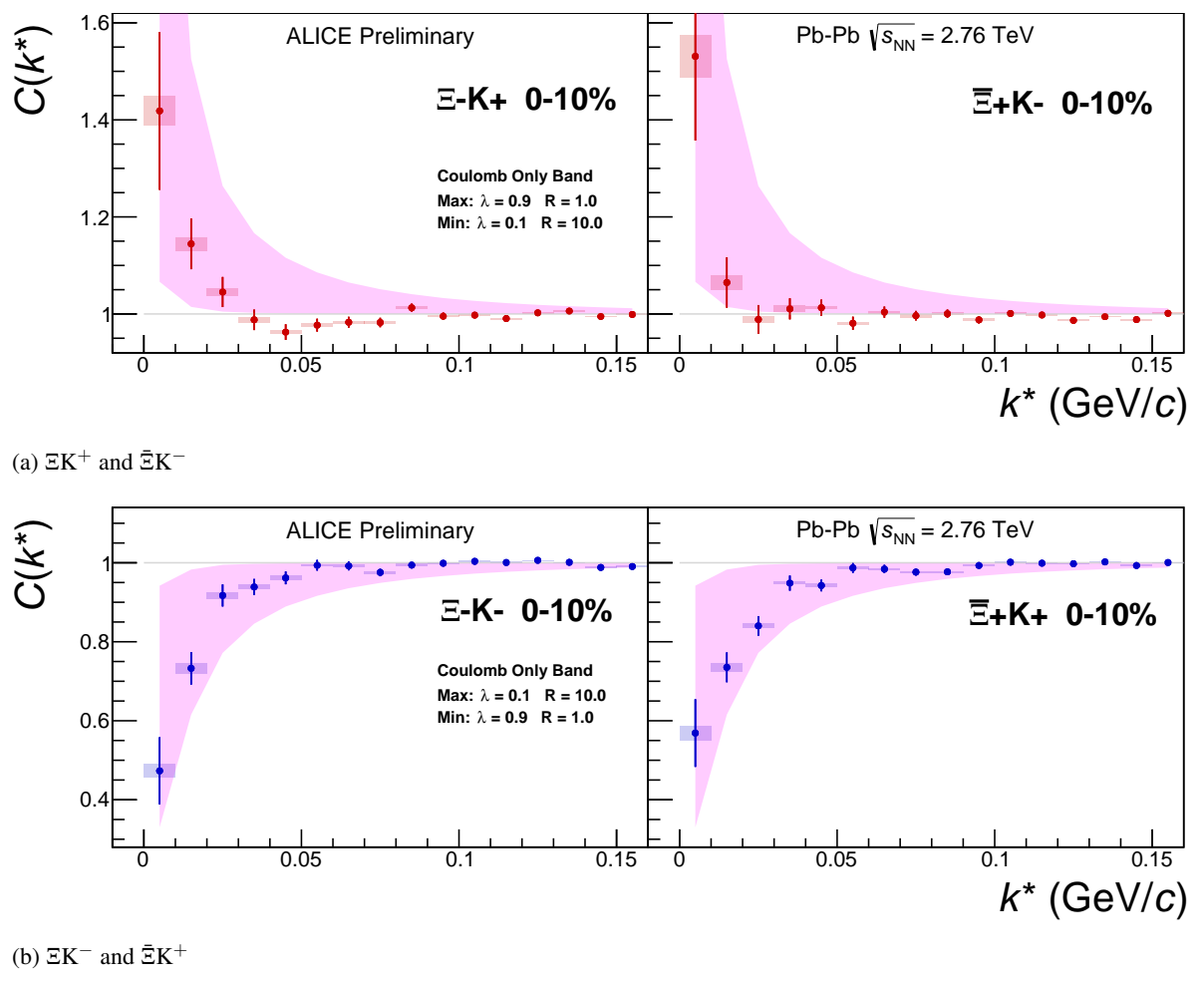
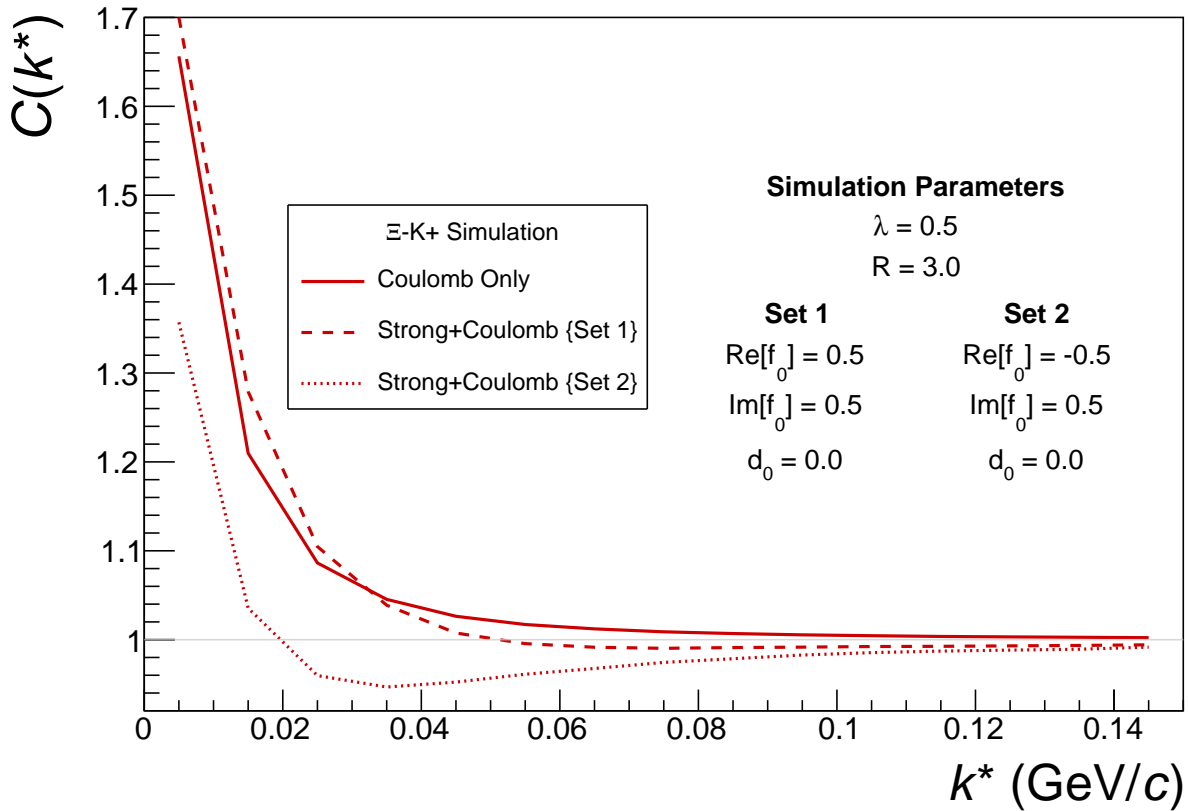
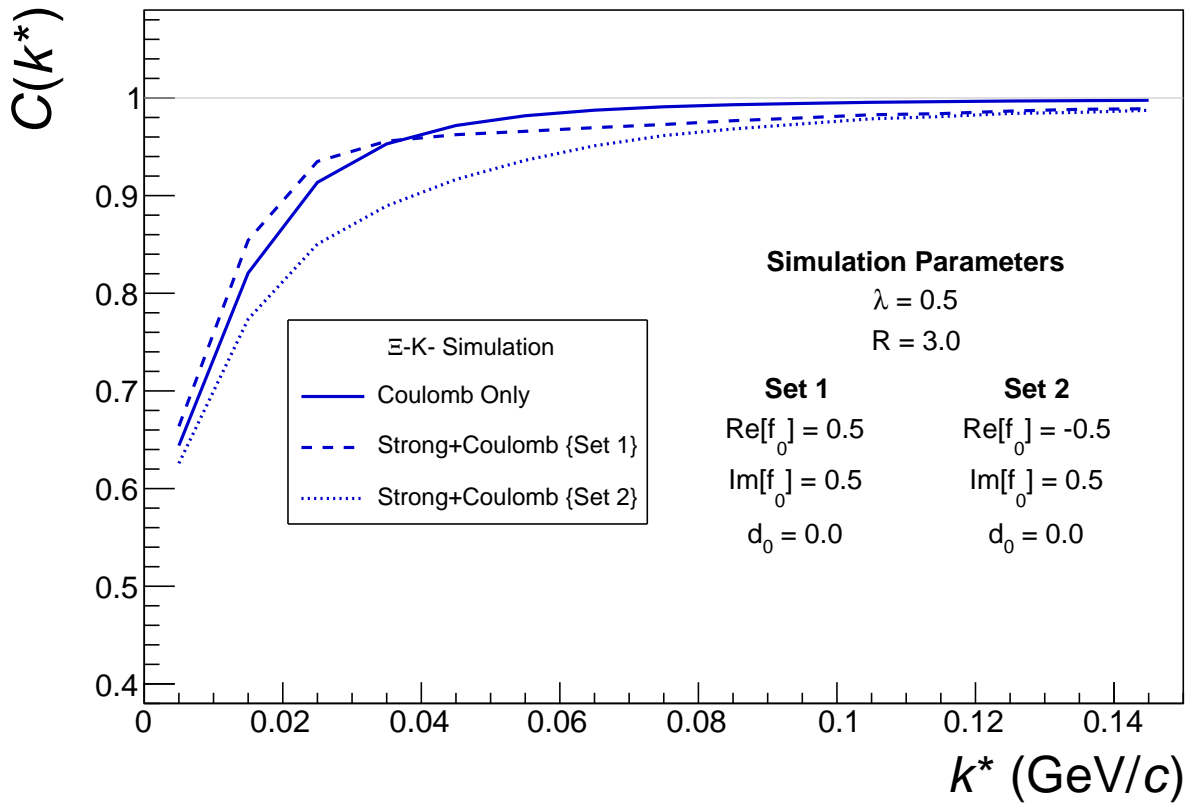


Fig. 26: ΞK^\pm Coulomb Only, 0-10% Centrality

(a) ΞK^+ and $\bar{\Xi} K^-$ (b) ΞK^- and $\bar{\Xi} K^+$ **Fig. 27:** ΞK^\pm Coulomb Only, 0-10% Centrality